Master's thesis

NTNU
Norwegian University of Science and Technology
Faculty of Information Technology and Electrical Engineering
Department of Electric Power Engineering

Kristoffer Fæster Klaussen

Voltage Stresses in Converter-Fed Electric Aviation Motors

A Finite Element Analysis

Master's thesis in Electric Power Engineering
Supervisor: Hans Kristian Høidalen
June 2020

NTNU
Norwegian University of Science and Technology

Kristoffer Fæster Klaussen

Voltage Stresses in Converter-Fed Electric Aviation Motors

A Finite Element Analysis

Master's thesis in Electric Power Engineering
Supervisor: Hans Kristian Høidalen
June 2020

Norwegian University of Science and Technology
Faculty of Information Technology and Electrical Engineering
Department of Electric Power Engineering

NTNU
Norwegian University of
Science and Technology

Problem Description

Electrification in aviation is a new field of application that implies severe restrictions on size and weight and requires optimum designs. Today, extra stress on machine windings comes from fast switching power electronics. This thesis focuses on the uneven voltage distribution occurring in the winding of inverter-fed motors. The tasks to be performed are:

- Perform measurements of voltage distributions in stator windings of the developed test object.
- Perform numerical or analytical calculations of the voltage distribution.
- Investigate the effect of reduced air-pressure at high altitudes.
- Propose required insulation thickness to withstand the voltage stresses and thus contribute to motor design optimization.

Supervisor: Prof. Hans Kristian Høidalen

Abstract

Inverter-fed drives (IFD) are vital in the transition towards more compact and lighter equipment in all-electric aircraft (AEA). However, IFD is known to cause detrimental effects within the turn insulation, due to short rise time. The high harmonic content of the inverter pulses causes the voltage distribution across turns to be determined by the capacitive coupling of the motor windings. This results in an unevenly distributed voltage, which stresses the first two turns substantially. This thesis examines the voltage distribution in windings subjected to short rise times by using analytical and finite element analysis. The thesis examines two different configurations: a simple 4-turn winding and a more complex 8-turn winding. The analytical method studies the equivalent capacitive circuits of the two configurations, where the initial voltage distribution is calculated, electrostatically. In FEM, 3D models of the two configurations are developed to examine the voltage distribution, which is based on transient electromagnetic waves physics. Individual parameter studies have been done to see how some essential parameters, such as insulation thickness, permittivity, and different grounding, affects the capacitive voltage distribution. The thesis shows that the FEM and analytical voltage distribution have correlating results in both configurations. However, the parameter studies show a more significant change in the analytical result than FEM. If the capacitances between turns are larger than the turn-to-ground capacitances, the voltage distribution becomes evenly distributed. The voltage distribution became more even by decreasing the turn insulation thickness and mainwall permittivity. Similar effects were shown by increasing the mainwall insulation thickness and turn insulation permittivity. Further investigations are needed to propose the required insulation thickness to withstand the voltage stresses. The breakdown strength of the insulation has to be calculated by considering both the overshoot from the cable and rise time and the uneven voltage distribution.

Sammendrag

Vekselretterforsyning er essensiell for utviklingen mot mer kompakt og lettere komponenter for helelektrisk fly. Vekselrettere er imidlertid kjent for å forårsake skadelige effekter i lederisolasjonen på grunn av kort stigetid på pulsene. De steile pulsene inneholder høye harmoniske som fører til at spenningsfordelingen i viklingen kun blir bestemt av viklingens kapasitanser. Detter resulterer i en ujevn spenningsfordeling gjennom viklingen, som stresser de to første vindingene vesentlig. Denne masteroppgaven undersøker den kapasitive spenningsfordelingen i viklinger ved å bruke FEM og analytiske beregninger. To forskjellige viklingskonfigurasjoner er sett på: en enkel 4-turns vikling og en mer kompleks vikling på 8-turns. Den analytiske metoden tar for seg den ekvivalente koblingen av de to viklingene, hvor den initielle spenningsfordelingen er beregnet elektrostatisk. 3D modeller av viklingene er utviklet i FEM for å studere spenningsfordelingen ved bruk av transient elektromagnetisk bølge fysikk. Individuelle parameterstudier er gjort for å se hvordan parametere som isolasjonstykkelse, permittivitet og forskjellig jord påvirker den kapasitive spenningsfordelingen. Resultatene viser at spenningsfordelingen i FEM og analytisk har lignende resultater i begge viklingene. Parameterstudiene viser derimot en mer signifikant endring i det analytiske resultatet i forhold til FEM. Hvis kapasitansene mellom vindingene er større enn kapasitansene mellom vinding og jord, blir spenningsfordelingen jevnt fordelt. Spenningsfordelingen ble jevnere ved å redusere lederisolasjonstykkelsen og permittiviteten til hovedisolasjon. Lignende effekter ble vist ved å øke isolasjonstykkelsen på hovedisolasjonen og permittiviteten til lederisolasjon. Ytterligere undersøkelser er nødvendig for å foreslå en optimalisert isolasjonstykkelse som kan motstå spenningsstresset. Holdfastheten til isolasjonen må da beregnes med hensyn til både oversving grunnet kabel og kort stigningstiden, i tillegg til den ujevne spenningsfordelingen.

Preface

This master's thesis concludes the two-year master program in Electric Power Engineering at the Norwegian University of Science and Technology. The thesis is carried out at the Department of Electric Power Engineering with support from engineers at Rolls-Royce Electrical Norway in Trondheim, and written during the spring of 2020.

I would like to thank my supervisors Hans Kristian Høidalen at NTNU and Njål Rotevatn at Rolls-Royce for their guidance, inspiring discussions, and help throughout this thesis's work. I would like to show my gratitude for the technical support provided by COMSOL, which made it possible to simulate the 3D models.

Trondheim, June 23, 2020

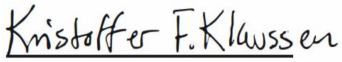

Kristoffer Fæster Klaussen

Table of Contents

List of Figures

List of Tables

Abbreviations

AEA All-Electric Aircraft.

FEM Finite Element Method.

HTS High-Temperature Superconductivity.

HV High-Voltage.

IEC International Electrotechnical Commission.

IFD Inverter-Fed Drives.

MEA More Electric Aircraft.

PD Partial Discharge.

PDIV Partial Discharge Inception Voltage.

PEC Perfect Electric Conductor.

PM Permanent Magnet.

pu Per Unit.

PWM Pulse-Width Modulation.

SiC Silicon Carbide.

t2g Turn-to-ground.

t2t Turn-to-Turn.

TEMW Transient Electromagnetic Waves.

VPI Vacuum Pressure Impregnation.

Chapter 1

Introduction

1.1 Background and Motivation

The reduction of emissions has been a globally focused goal in the last decades. Especially, the transportation industries have felt the push to transition from using fossil-fuel to greener and more economically friendly alternative energy sources. The aviation industry is responsible for 2 – 3 % of the emissions globally and is still increasing. International regulations have been set, which requires airlines to reduce the extension of emissions [1].

The concept of the more electrical aircraft (MEA) has consisted since the 1970s to replace pneumatic, mechanical and hydraulic systems with electrical power [2]. The push towards all electrical aircraft (AEA) has been increasing proportionally with the improvements in technology in the last decades. However, a complete electric propulsion system is not nearly mature enough to replace the traditional jet engines in commercial flights. The current limitations which make AEA currently infeasible regarding long-distance commercial flights, are mainly the propulsion method and battery capacity, having insufficient power density.

Reducing the weight and volume of all components within the electric propulsion system will help tremendously. However, there is a trade-off question in every attempt to improve. As an example, factors such as higher frequency and faster power electronic switching will introduce high-speed motors and inverters, which are more compact and lighter [3]. This introduces the need for more cooling as the temperature will increase significantly. Inverter-fed drives (IFD) is unavoidable in MEA and AEA electric systems. However, IFD is known to cause detrimental effects within the turn insulation of the motor windings, which can cause premature motor failure. Effects such as high voltage overshoot at the motor terminals and uneven voltage distribution across turns are examples of this. The insulation system in electrical machines takes up much space and plays a significant role in the sizing of a machine. Although the insulation system is the weakest link, it is unavoidable; if the insulation fails, the whole machine will have a complete breakdown. Usually, these effects have been reduced by filters and other preventative methods in systems where volume and weight of the holistic system have no boundaries.

1.2 Scope of Work

This thesis focuses on inverter-fed motor windings meant for electric aircraft systems: Turn insulation stress due to non-uniform voltage distribution.

The scope of work includes:

- Modelling of 3D coils in FEM for voltage distribution simulations
- Analytical voltage distribution calculations
- Comparison analysis of the two methods used

Limitations of the work include:

- Testing of the developed test object in laboratory

Also, the FEM and analytical study's simplifications and approximations are justified in the methodology chapter of the respective methods.

The Transition from the Specialization Project

The specialization project, which was a pre-work to this thesis, consisted mainly of a literature survey around the stresses subjected to the insulation system of form-wound windings [4]. The pre-work considers all four TEAM stresses and all insulation components of a type II insulation system and gives an overview of these components' ageing and failure mechanisms. In addition, the pre-work gives an overview of type II insulation systems' testing procedure in accordance with IEC 60034-18-42 and recent investigations that challenge the standard. FEM simulations were briefly introduced.

This thesis will concentrate more on the turn insulation and the uneven voltage distribution due to the inverter's fast rise times. Thus, some of the most important features regarding this covered by the specialization project will be presented in this thesis also. The main methodology used in this thesis are FEM and analytical calculations of voltage distributions inside motor windings.

1.3 Thesis Outline

- **Chapter 1 - Introduction**: describes the motivation and background for this master thesis. Followed by the scope of work and limitations of the objectives.
- **Chapter 2 - Literature Survey**: gives a review of relevant research of more electric aircraft and all electric aircraft, research of standard testing proposals in IEC 60034-18-42 and lifetime investigations. In addition, relevant information of copper wiring is presented.
- **Chapter 3 - Voltage Stress in Inverter-Fed Motors**: describe how the stress in the motor windings is generated and the effect it has.
- **Chapter 4 - Methodology**: presents the work done in this thesis in form of the analytical and by FEM study.
- **Chapter 5 - Results**: presents the results from the two different study methods and a comparison between them. In addition, a parameter study is conducted.
- **Chapter 6 - Discussion**: gives a reflection around four main different discussion points.
- **Chapter 7 - Conclusion**: includes the most important findings in this master thesis.
- **Chapter 8 - Further Work**: introduces suggestions to further investigations.

Chapter 2

Literature Survey

2.1 Electrification in Aviation

As mentioned introductory, there are massive benefits to have the aviation industry electrified. The main reason is the reduction of NO_x and CO_2 emissions; the aviation industry stands for 2 – 3 % globally. Other benefits such as improved efficiency and lower costs over time are also important features for this movement. Of course, this can not change rapidly due to the lack of maturity of the technology required.

2.1.1 More Electric Aircraft

The recent decades, more electric aircraft (MEA) has been the approach to improve application systems in aircraft. Auxiliary systems that traditionally have been powered by hydraulic, pneumatic, and mechanic power sources have been replaced by electric systems [3, 5]. There are many benefits from these exchanges, such as efficiency, redundancy, and reliability. Power electronics have been vital in the evolvement of MEA, where most of the electrical system traditionally had fixed frequency and voltage are now varied from 350 – 800 Hz at 115 or 230 V_{AC} [3]. More importantly, electrical systems introduce a variety of advanced prognostics and diagnostics in all systems, which could improve availability and reduced unscheduled maintenance of aircraft [5]. Operating data from the aircraft can be used to improve the systems and technology further.

Still, there is a long way to go to replace the jet engines in commercial aircraft.

2.1.2 All Electric Aircraft

There are currently two limitations which make it impracticable to have long-distance commercial AEA: electric propulsion sources and batteries.

Electric Propulsion Methods

Electric propulsion refers to a propulsion system driven by electric motors. Generally, motors meant for commercial AEA are preferred to have high mechanical speed since

it will decrease weight and volume. Due to power electronics, induction machines with high inrush current can be replaced by permanent magnet (PM) machines, which have higher power density and efficiency compared to induction machines. Additionally, synchronous machines do not require a supply of rotor current [3]. Motors with high temperature superconducting (HTS) materials are considered a promising candidate for future AEA. A fully superconducting machine can potentially achieve three times lower mass than turbofan engines, due to the reduction of field and armature winding losses [6]. However, such high temperatures require sufficient cooling systems.

Batteries

The most significant improvement required is the battery technology. The advantages with battery as the energy source is regarding emissions and efficiency. However, there are several known disadvantages; for example, the battery's weight is constant during flight, while fuel-driven aircraft reduces weight proportionally with the fuel-burning. Besides, the specific power is low, as can be seen in figure 2.1.

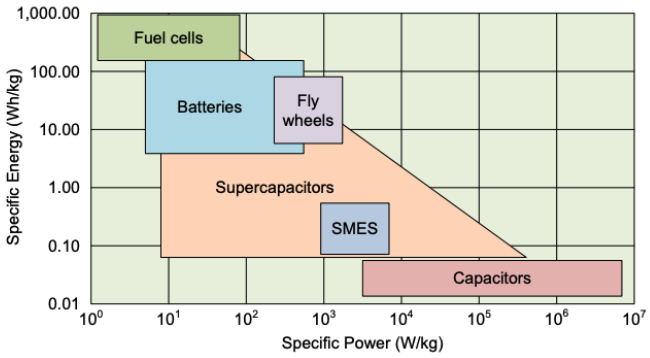

Figure 2.1: Ragone chart [7]

There is a distinction between specific power (W/kg) and specific energy (Wh/kg), whereas batteries have high specific energy but low specific power. Although the specific energy of batteries is high, the release of energy is slow; thus, batteries are more suited to offer range at low speed than acceleration and high speed [8]. Nevertheless, the future looks promising with the energy density of metal-air batteries, theoretically [8, 9]. This can be seen in figure 2.2, where Fe-Air has considerably more potential than gasoline, theoretically.

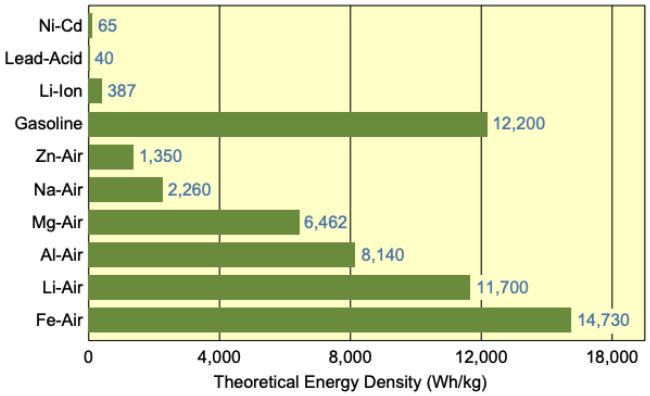

Figure 2.2: Theoretical specific energies of batteries compared to gasoline [9]

2.2 Dielectric Materials

2.2.1 Lifetime Investigations

The pre-work done by the author gave a literature survey on the testing of type II coils, according to IEC 60034-18-42 [10]. However, regarding MEA/AEA, higher standards of safety precautions have to be taken, thus stricter requirements in lifetime estimations. With this in mind, the IEC 60034-18-42 could be considered too polite and optimistic in the testing procedure of the insulation system meant for an electric aircraft system.

The proposed test sample of IEC/TS 60034-18-42 is a general approach that considers two insulated strands covered by main insulation tape, depending on the material. The PDIV and lifetime exponent have shown higher results than the whole coil with the same properties [11].

The standard IEC 60034-18-42 also addresses sinusoidal and impulse voltage with equal peak to peak voltage and frequency as the inverter pulses, at least up to 1 kHz, as the approach to test the lifetime of the insulation [10]. Regarding the rise time, the square wave voltages generated by the inverter are significantly different from sinusoidal voltages with similar peak-peak voltage and frequency. This difference enlarges with a shorter rise time. Wang, Cavallini and Montanari have investigated this, where the sinusoidal voltages estimated the lifetime more optimistically [12]. Hence, the square wave voltages with similar rise times generated by the inverter are recommended for more accurate lifetime estimation.

Moonesan et al. [13] have investigated the time to failure of various turn insulations and methods under PWM voltage waveforms. The source used here is a high voltage PWM generator supplying unipolar PWM pulses of 3kHz and a fundamental frequency of 60 Hz. Peak voltage and rise time of pulses are 12 kV and 250 – 300 ns, respectively. The samples from their study are in accordance with IEC 60034-18-42, which may yield higher PDIV and lifetime exponent, according to [11]. Epoxy resin is filled in

the space of the bent region of the sample to prevent premature failure by PD. The insulation types investigated are shown in table 2.1

Table 2.1: Turn insulation samples investigated in [13]

Insulation Group	Turn Insulation	No. of Layers and Lapping	Nominal Thickness (pu)
A	Mica/Film	1 layer, 1/2 lap	2.7
B	Mica/Film	1 layer, 1/3 lap	1.3-2.7
C	Mica/Film	2 layers butt lap	2.7
D	Daglas	N/A	1.7
E	Daglas	N/A	2.5
F	Enamel I	N/A	1
G	Enamel II	N/A	1
H	Enamel + Mica Glass Turn Tape	1 layer, 1/2 lap	4.2

Each insulation group is tested with five samples to obtain a Weibull probability plot of the lifetime. Group H is not considered in the result due to its inability to fail within 50000 minutes. Part of the reason for this could be the type of insulation. The other part is most likely the thickness, which is almost doubled compared to the other in pu. From those insulation groups that did fail, the Mica/film groups showed a clear advantage compared to the other insulation groups. The authors highlight that group A and C had significant differences in time to failure even though the nominal thickness is the same, and discusses that this could be due to the lapping configuration. Group A did only fail in the crotch area of the sample, whereas the others failed in the straight part. Another observation from the authors is that the failure occurred mostly at the edge between the strands, where the stress is higher in addition to the possibility of air pockets. Bad VPI will also affect the result significantly.

Table 2.2: Time-to-failure result in minutes [13]

Sample #	Insulation Group						
	A	B	C	D	E	F	G
1	10080	1510	5010	20	24,5	0,42	59,5
2	9810	462	2730	5	34	1,36	104
3	17546	357	1526	21	15	0,98	67
4	14546	844	3810	18	33	1,19	127
5	14530	473	3300	10	10	0,72	142,5

The study concludes that some mixture of mica insulation will be most effective in obtaining sufficient lifetime under PWM voltage waveforms.

Researchers from ABB [14] have investigated the lifetime of mica-based insulation in HV machines subjected to converter-like voltages. This study is more towards the drive side, how a change from 2-level to multilevel converter will affect the ageing of mica-based machine insulation, and which method is best fitted to represent the multilevel voltages. The test sample here is also a pig-tail, although only one of the conductors is insulated. The conductors are wrapped at the straight midsection with mica tape

and surface tape. This study concludes that the multilevel converter voltages are best represented by a fitted sinusoidal envelope voltage to predict the correct lifetime, and that the peak to peak voltage and fundamental frequency is related to the ageing rate of the insulation.

Chapter 3

Voltage Stress in Inverter-Fed Motors

Inverter-fed drives (IFD) have become more and more popular over the last decades due to its many advantages, such as high efficiency, controllable frequency and magnitude, to name a few. However, it comes with a cost, which can lead to premature failure of the insulation system. This chapter will present the origin of the voltage stresses and their effect on the turn insulation.

3.1 What causes the stress?

The process of developing a controllable signal starts by rectifying the incoming alternating voltage and smoothing it to a DC link using a rectifier and a capacitance. Further, the DC link gets chopped by fast power electronic switches in the inverter to provide a pulse width modulated voltage. An approximate sinusoidal output is then obtained with controllable magnitude and frequency at the motor terminal, as shown in figure 3.1 for a single phase.

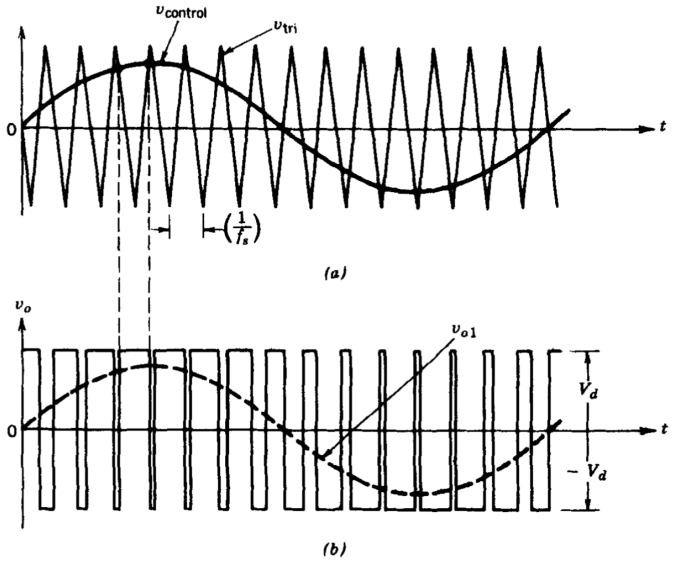

Figure 3.1: Pulse width modulation with bipolar voltage switching [15]. a) control signal, b) voltage output

Figure 3.1a shows how the PWM voltage pulses are made by generating a triangular waveform, v_{tri}, and comparing it to a sinusoidal control signal, $v_{control}$, with the desired frequency, which is equal to the frequency of the output signal. The frequency of the triangular signal is the switching frequency of the inverter, f_s, also called carrier frequency. Figure 3.1b is the voltage impulses that switches between $\pm V_d$, which is the DC link voltage. v_{o1} is the dominant fundamental frequency component at the inverter output. The lowest harmonic component is at the PWM switching frequency. A more detailed explanation is provided by [15].

Drive designers will generally aim for the highest practical switching frequency due to its many benefits, such as smaller equipment. Towards AEA, it is desired to achieve higher temperature capabilities, reductions in weight and volume, and efficiency improvements. Silicon carbide (SiC) is a promising material for use in aircraft power electronics and can open several doors of feasibility in aircraft power systems in the near future [3]. For instance, SiC MOSFETs have fast switching and high efficiency due to low switching losses. However, fast switches like SiC MOSFETs shortens the rise times as well.

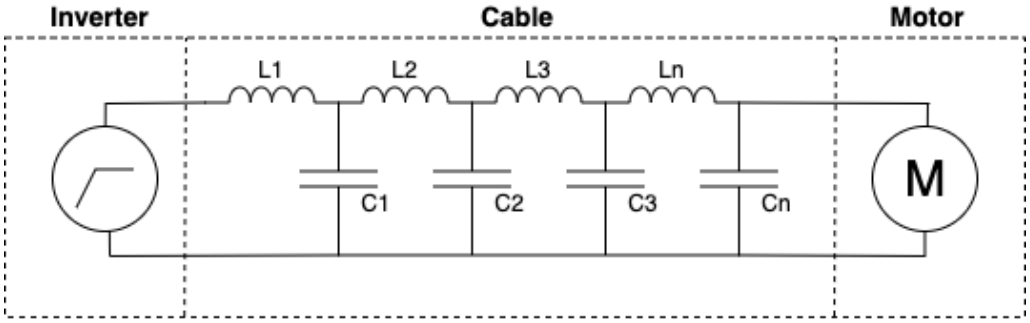

Figure 3.2: Transmission line representation of the feeder cable between inverter and motor

Furthermore, the output voltage pulses are transmitted through a feeder cable to reach the motor terminals. The feeder cable between the converter and motor terminals will act as a transmission line for the pulses [16]. The cable can be represented as sections of pi-equivalents, determined by capacitances and inductances, as shown in figure 3.2 for a single phase. Because of the short rise time of the pulses and the that the IFD has to charge up the cable capacitances and inductances for each rising edge, the pulses may change in shape along the cable, causing a voltage overshoot at the motor terminals.

The technical report from GAMBICA/REMA [17] depicts how the pulse along the cable acts.

- Figure 3.3 shows the pulse at the exit of the drive and entrance of the cable. The pulse enters the cable at $t = 0$ and reaches V_d at t_r, which is the rise time. This is an idealized example where the rise time t_r is smaller than the propagation time in the cable t_p.

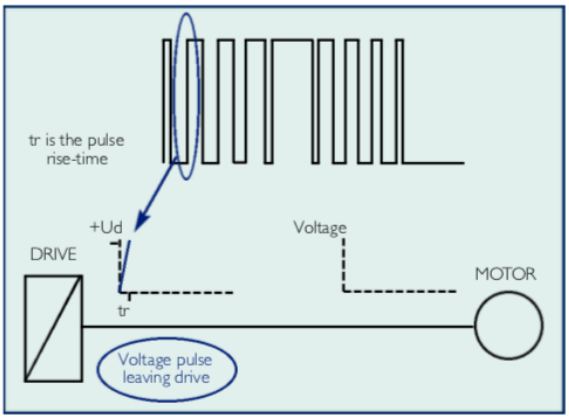

Figure 3.3: Pulse at rising edge at the drive side, t is in the interval $[0, t_r]$

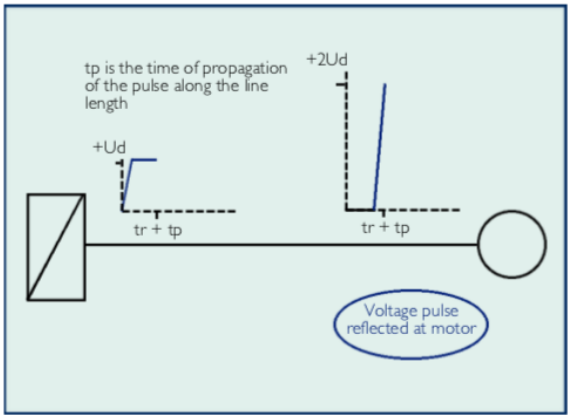

Figure 3.4: Pulse after on propagation. t in the interval $[t_r, t_r+t_p]$

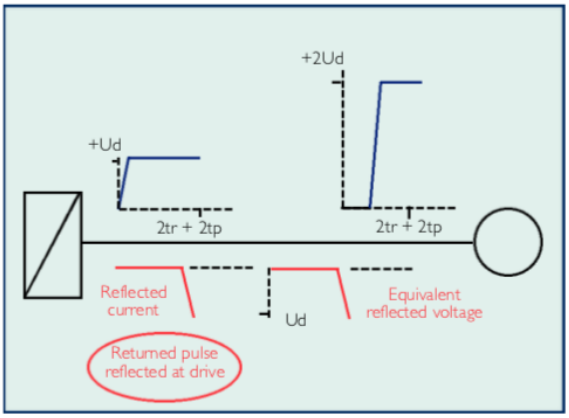

Figure 3.5: Reflected pulse has propagated backward with a negative polarity, t in the interval $[t_r+t_p, 2t_r+2t_p]$

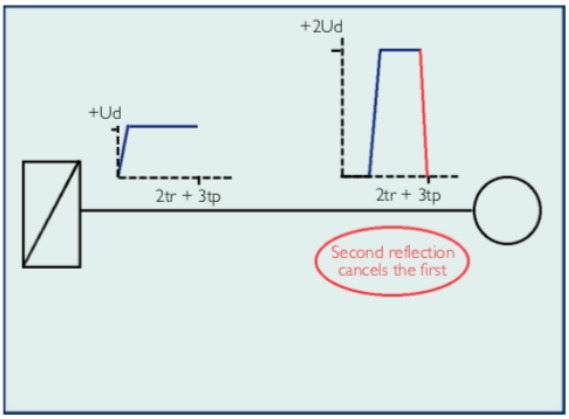

Figure 3.6: Pulse propagates towards the motor terminals. t in the interval $[2t_r+2t_p, 2t_r+3t_p]$

- Figure 3.4 is the case where the pulse has propagated along the cable and reached the motor terminals, which is at $t = t_r + t_p$. The pulse reflects as it reaches the motor terminal due to the mismatch between cable and motor impedances. As a result, the pulse can exceed the original peak magnitude, in this example, up to 2 pu.
- Figure 3.5 shows the case where the reflected pulse has reached the drive side of the cable, $t = 2t_r + 2t_p$. The impedance of the drive is very low; the reflection coefficient is thus approximately -1. This leads to the 2pu pulse to drop to the original peak. However, the reflected current is negative, which results in a negative voltage pulse when returning along the cable.
- In figure 3.6, at $t = 2t_r + 3t_p$, the second reflection at the drive's end is shown, where the pulse has propagated towards the motor terminal again. The reflected pulse with negative polarity counteracts the voltage increase at the motor terminal, such that the second reflection cancels the first.

For an idealized example like this, the voltage would oscillate indefinitely due to no losses, which results in 100 % reflection. Practically, there are high-frequency losses

in the cable causing the waveforms to be rounded, which decays the peak voltage for each reflection until it is stabilized at the DC-link value [17]. In the example shown in figure 3.3-3.6, t_p is larger than t_r. However, if the cable is shorter such that $2 \cdot t_p < t_r$, then there will not be any overshoot at the motor terminals. Thus, the overshoot at the motor terminals is mainly dependent on the cable length and rise time.

The maximum cable length or the minimum rise time can be calculated for a given voltage overshoot by using the method described by von Jouanne and Enjeti [18].

The propagation time t_p, which can be found by

$$t_p = \frac{l}{v} \tag{3.1}$$

where l is the length of the cable and v is the pulse velocity

$$v = \frac{1}{\sqrt{LC}} = \frac{1}{\sqrt{\mu\varepsilon}} = \frac{c}{\sqrt{\varepsilon_r}} \tag{3.2}$$

The impedance mismatch is defined by the reflection coefficient Γ_m, as seen in equation 3.3.

$$\Gamma_m = \frac{Z_m - Z_0}{Z_m + Z_0} \tag{3.3}$$

where Z_m and Z_0 represent the motor and cable surge impedance respectively. The reflected voltage wave at the motor terminal is given by the following, depending on whether t_p is smaller or larger than t_r:

$$V_m = \frac{t_p \cdot V_d \cdot \Gamma_m}{t_r} \quad \text{for} \quad t_p < t_r \tag{3.4}$$

and

$$V_m = V_d \cdot \Gamma_m \quad \text{for} \quad t_p \geq t_r \tag{3.5}$$

where V_d (U_d in figure 3.3-3.6) is the DC link voltage of the inverter. The reflection coefficient at the drive side of the cable is given by

$$\Gamma_i = \frac{Z_i - Z_0}{Z_i + Z_0} \tag{3.6}$$

where Z_i is the impedance of the inverter. The final peak voltage at the motor terminal can then be determined:

$$V_{m(peak)} = \frac{3 \cdot l \cdot V_d \cdot \Gamma_m}{v \cdot t_r} + V_d \quad \text{for} \quad t_p < \frac{t_r}{3} \tag{3.7}$$

and

$$V_{m(peak)} = V_d \cdot \Gamma_m + V_d \tag{3.8}$$

where 3 represents the number of times the pulse has travelled the length of the cable. For short cables where $t_p < \frac{t_r}{3}$, the ratio between peak voltage and dc link voltage can be described as:

$$\frac{V_{m(peak)}}{V_d} = \frac{3 \cdot l \cdot \Gamma_m}{v \cdot t_r} + 1 \tag{3.9}$$

where

$$\frac{3 \cdot l \cdot \Gamma_m}{v \cdot t_r} \tag{3.10}$$

determines the overshoot. The critical cable length can then be calculated for a given maximum voltage overshoot and rise time. For example, an overshoot of 10%, a typical PVC-insulated cable with propagation velocity of $1.7 \cdot 10^8 \frac{m}{s}$ and rise time of $0.1 \mu s$.

$$l = \frac{0.1 \cdot 1.7 \cdot 10^8 \frac{m}{s} \cdot 0.1 \cdot 10^{-6} s}{3 \cdot \Gamma_m} = 0.57 m \tag{3.11}$$

The motor impedance is assumed so high compared to the cable impedance that the reflection coefficient is approximately 1. The same can be done for critical rise time, for a given cable length and a maximum voltage overshoot.

Thus, to prevent this from happening in electric motors in aircraft, it is recommended to have the inverter as close as possible to the motor terminals. Filtering is the most common way of reducing this problem. However, filters take up space and weight, which is not preferable.

3.2 Voltage Distribution

As clarified, there is a substantial possibility that the motor terminals will experience overshoot in voltage if the cable is long and the rise time short. M. Kaufhold et al. have shown that the voltage distribution is inductive and/or capacitive, depending on the rise time [19].

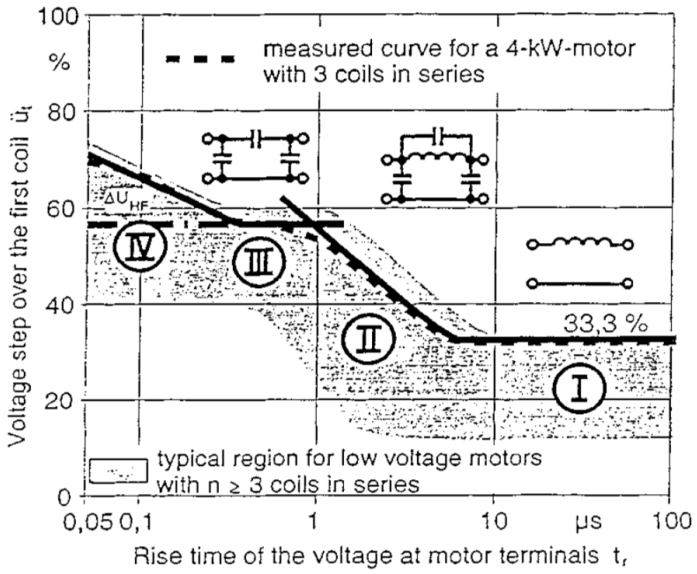

Figure 3.7: Distribution mechanism of the transient voltage step over the first coil [19]

They have distinguished four characteristic ranges, as illustrated in figure 3.7:

- I: Very long rise times, only inductive couplings are effective, and the voltage distribution is distributed evenly. $t_r > 10\ \mu s$
- II: Inductive and capacitive couplings behave similarly to that of transmission lines. $1\ \mu s < t_r < 10\ \mu s$
- III: Short rise times, typical for PWM inverters, the transient voltage distribution is determined primarily by capacitive couplings, which results in uneven distribution. $200\ ns < t_r < 1\ \mu s$
- IV: Rise times shorter than 200 *ns*, portions of the windings can be excited to HF oscillations.

The steep rising edge of the pulses contains a high harmonic specter of frequencies. The equivalent frequency of the steep pulse edges can be calculated by using equation 4.9. Thus, shorter rise time gives higher frequency, which gives less inductive involvement in the equivalent circuit of the winding. This can be seen in equation 3.12; the inductive reactance gets so large that it will act as a closed valve.

$$\omega L >> \frac{1}{\omega C} \tag{3.12}$$

Thus, the voltage in the winding is distributed unevenly across turns during the switch commutation. The uneven voltage distribution and high voltage overshoot at the motor terminal will result in a higher level of electric stress, which can exceed the PDIV. Consequently, this accelerates the degradation of turn insulation significantly, which can cause premature failure. Due to the detrimental environment, turn insulation failure has become a root cause of machine failures over the years [20–22]. The uneven voltage distribution effect can also be seen across coils in series [23–25].

As shown, studies have considered the rise time and cable length as the only factors affecting the pattern of the voltage distribution. Other parameters, such as pulse width has also shown to be significant in shaping the pulse pattern [23, 26].

The motor windings subjected to other surges similar to those of the inverters but more fatal. Examples of these transients can be:

- Lightning
- System faults
- Motor CB closing/opening

Anyhow, these surges are nonrecurring and will not cause gradual deterioration. There will either be no effect or immediate failure. A breakdown will occur if the amplitude of the transient voltage surge is higher than the breakdown strength of the insulation.

3.3 Partial Discharge

The Type II insulation system referred to in IEC 60034-18-42 [10] will most likely experience partial discharge during its lifetime. As mentioned, interturn insulation can reach voltage levels where PD may occur. PDs occur if the insulation contains cavities of air, which can exist due to degradation or bad VPI process. If so, the PDs will erode through the turn insulation, causing a turn-to-turn failure, which further melts the mainwall insulation causing complete failure of the machine.

The essential pulse characteristics presented, such as rise time, pulse width, and repetition rate, will impact the PD properties. Dr. Moghadam et al. [26] showed that increased rise time gave reduced PD magnitude, but an increase in appearance. Similarly, this occurred by increasing the repetition rate as well.

A simple analysis of the electric stress magnitude occurring in air cavities can be done by using the ABC-model. Figure 3.8 illustrates a dielectric material containing a void.

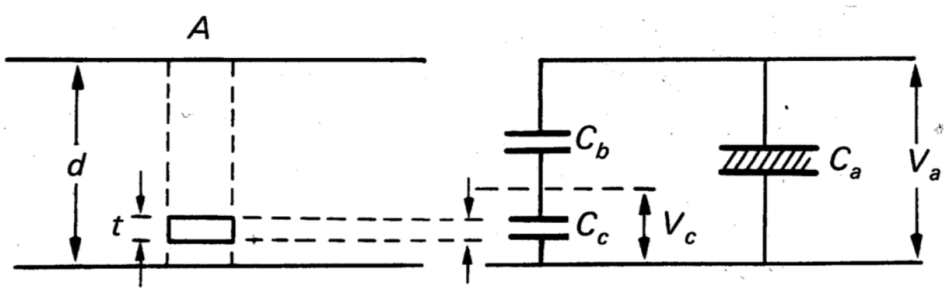

Figure 3.8: ABC-model [27]

By considering the section where the cavity exist and assuming parallel plate geometry,

the capacitances C_c and C_b can be found:

$$C_b = \frac{\varepsilon_r \varepsilon_0 A}{d - t} \tag{3.13}$$

$$C_c = \frac{\varepsilon_0 A}{t} \tag{3.14}$$

where

C_c : Capacitance of the void
C_b : Capacitance of the dielectric in series with the void
C_a : Capacitance of the remaining dielectric
A : Surface of parallel plate
t : Thickness of the void
d : Thickness of the dielectric

The voltage across the void can be found by voltage division of the capacitances:

$$V_c = V_a \cdot \frac{C_b}{C_b + C_c} = \frac{V_a}{1 + \frac{1}{\varepsilon_r}(\frac{d}{t} - 1)} \tag{3.15}$$

where V_a could be considered the interturn voltage.

3.3.1 Partial Discharge Inception Voltage

There is a close relationship between PD behavior and failure behavior. Thus, to achieve a sufficient lifetime of the insulation, the stress level must always stay below the PDIV [19, 20]. That is why all qualification tests shall be performed above the PDIV level, on the premise that premature failure is caused by PDs [10]. However, the PDIV is not a fixed value throughout the insulation lifetime, which is similar to the breakdown strength; it will weaken over time. Due to this, several studies have focused on the impact different designs have on the PDIV.

Temperature and pressure are known to impact the PDIV with regards to Pachen's curve. This is confirmed by an experimental study that tests a motor mounted in a vacuum chamber with varying pressure [25]. Additionally, VPI process, turn insulation thickness, and copper strand thickness have demonstrated an effect regarding the PDIV [26, 28].

Chapter 4

Methodology

This chapter presents the methodology of the studies done in this thesis. First, the winding configurations studied and its dimensions will be presented. Next, the methodology is divided into two sections based on the study: Analytical study and finite element method (FEM). COMSOL Multiphysics®is used as FEM software.

4.1 Winding Configurations

Two winding configurations are examined: a simple 4-turn winding and a more complex 8-turn winding. Both windings are form-wound windings with rectangular copper wires. Mica tape insulation is considered for both turn and mainwall insulation, whereas the turn insulation consists of four layers 0.1 *mm* tape and mainwall three layers of 0.15 *mm* tape. Such details are not crucial for the modelling of the insulation system, except for the total thickness and permittivity. They are instead discussion points to be reflected in chapter 6.

4 – Turn Winding

The purpose of the 4-turn winding is to study the effect of changing parameters regarding the capacitive voltage distribution more easily. The windings are wound next to each other, which can be seen in figure 4.1, where the cross-section is illustrated.

8 – Turn Winding

This winding is a more complex configuration, which consists of two layers 4-turn windings wound oppositely on top of each other. In this configuration, additional insulation can be placed between the two layers if necessary, regarding stress between the upper and lower layer. An equivalent circuit of this winding composition is shown in the analytical study and a 3D model in the FEM study, figure 4.4 and 4.8, respectively.

4.1.1 Dimensions

The dimensions in table 4.1 represent the base case of the two winding configurations.

Table 4.1: Parameter base-values of figure 4.1

Description	Parameter	Value
Conductor height	h	5 mm
Conductor width	w	4 mm
Mainwall insulation thickness	δ_m	0.45 mm
Interturn insulation thickness	δ_t	0.8 mm
Length of slot	L	300 mm
Relative permittivity	ε_r	3

The relative permittivity is considered equal in both insulation components in the basis case. The interturn thickness is equal to twice the conductor insulation thickness. The thesis focuses more on the interturn parameter since this determines the distance between the conductors, which will be stressed. A cross-sectional representation of the 4-turn winding is shown in figure 4.1, which depicts the components and parameters involved. The boundaries to ground can also be seen in this figure, which is represented by the stator core. Thus, ground is present at the sides and bottom of the mainwall insulation, while the top is open towards air. This grounding applies for the 8-turn winding also.

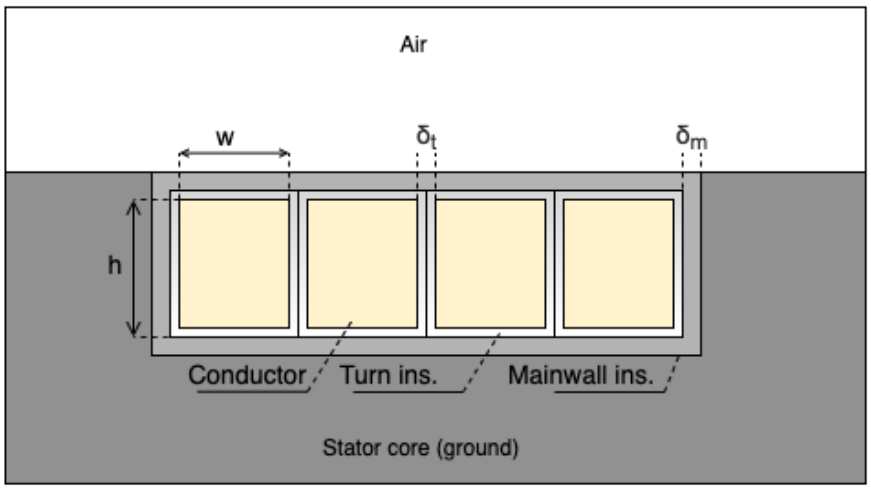

Figure 4.1: Cross-section of a slot showing the parameters of the 4 turn winding

4.2 Analytical Study

The analytical study is based on the theory presented in section 3.2, that short rise time of PWM voltages results in such high frequency that the capacitive coupling of the winding determines the initial voltage distribution at the motor terminals. This section presents the capacitance calculation method, an overview of the equivalent circuits, constraints and the method of finding the analytical voltage distribution.

4.2.1 Maxwell Capacitance Calculation

This section presents the capacitance calculation method, which calculates the capacitances in all analytical study cases. The former method of calculating the capacitances, as addressed in the pre-work, was quite cumbersome and time-consuming [4]. The method presented by Friedel [29] has a clear advantage in calculating capacitances in complex winding configurations. Hence, this method is used to calculate the capacitances in all analytical study cases in this thesis.

Theory

The Maxwell capacitance matrix describe the relation between the charge of the i-th conductor to the voltages of all conductors in a system. This is based on the definition

$$Q = C \cdot V \tag{4.1}$$

where

Q : Charge vector
C : Maxwell capacitance matrix
V : Voltage vector

This can also be done by summarizing the mutual- and self-capacitances, where the total charge on i-th conductor is

$$Q_i = C_{ii,m} \cdot V_i + \sum_{i \neq j}^{n} (C_{ij,m} \cdot (V_i - V_j))$$

where m indicates that these are mutual- and self-capacitances, which are the actual capacitances.

$$\begin{bmatrix} Q_1 \\ Q_2 \\ \vdots \\ Q_n \end{bmatrix} = \begin{bmatrix} C_{11} & C_{12} & \dots & C_{1n} \\ C_{21} & C_{22} & \dots & C_{2n} \\ \vdots & \vdots & \ddots & \vdots \\ C_{n1} & C_{n2} & \dots & C_{nn} \end{bmatrix} \begin{bmatrix} V_0 \\ V_1 \\ \vdots \\ V_n \end{bmatrix} \tag{4.2}$$

The coefficients of this matrix are found by measuring the charge on the $i-th$ conductor when the potential at the same conductor is equal to 1, and all others are grounded. The Maxwell matrix is also called the ground capacitance matrix [29]. One of its

identities are that the non-diagonal capacitances is negative. The relations between mutual and Maxwell matrix are the following:

$$C_{ij,m} = -C_{ij} \tag{4.3}$$

$$C_{ii,m} = C_{ii} + \sum_{i \neq j}^{n} C_{ij} \tag{4.4}$$

Feature in COMSOL Multiphysics ®

Electrostatic physics is used here to calculate the capacitances. The cross-sectional slot segment of the winding is built with the desired parameter values. Figure 4.2a and 4.2b illustrate the 2D geometry of the windings used to calculate the base case of the 4-turn and 8-turn winding, respectively. The sides and bottom of the mainwall insulation are grounded in both configurations, which represents the stator core similar to figure 4.1.

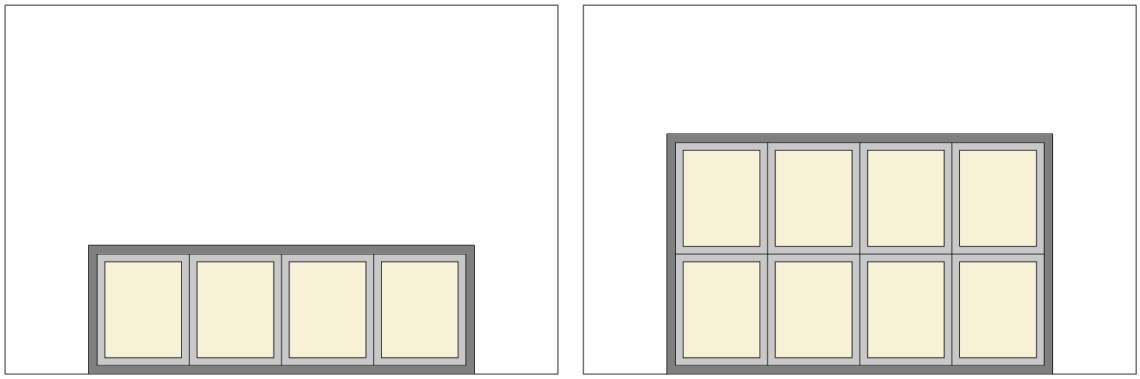

(a) 2D figure of the 4-turn winding **(b)** 2D figure of the 8-turn winding

Figure 4.2: 2D geometries used to calculate the Maxwell capacitance matrix for each respective winding model

Each conductor corresponds to a terminal boundary with the potential of 1. By performing a parametric sweep in the study, the terminals can be excited with the potential of 1, one at a time, while the other terminals will act as grounded terminals. The Maxwell capacitance matrix can then be calculated since it is a post-processing feature in COMSOL Multiphysics ®.

4.2.2 Capacitive Coupling

The capacitive coupling which determines the voltage distribution for short rise times is presented here for each winding configuration.

Constraints

Constraints and simplifications done for both winding models are:

- Losses and mutual inductances are neglected since the capacitances determine the voltage distribution, initially.

- Proximity and skin effect are not considered since such level of accuracy is not needed to achieve an estimate of the expected voltage distribution. By neglecting these effects simplifies the equivalent representation of the winding considerably.
- The analytical model considers the slot-section only, as illustrated in figure 4.1. Realistically, the overhang sections have different properties than the slot sections, much due to the environment since the stator core is not present, traditionally.
- The capacitances between turns are equal. This applies mostly to the 4-turn winding. This is partly true for the 8-turn winding since it has several sets of t2t capacitances: The capacitances between the upper adjacent turns, capacitances between the lower adjacent turns and capacitances between vertically adjacent turns. Each set has 3 or 4 equal capacitances.
- Only adjacent t2t capacitances are considered since the windings are form-wound, thus contribution to turns that are not adjacent can be neglected.

Turn-to-Turn Capacitance

The turn-to-turn capacitances are determined by the interturn insulation thickness, relative permittivity and conductor dimension. If the capacitances between turns are small, compared to the capacitance to ground, the voltage will be distributed unevenly over the winding [24, 30]. Thus, to get a more ideal and even distribution under short rise time conditions, the capacitance between turns must be larger than the t2g capacitance.

For comparison, the t2t-capacitance has been calculated by using the parallel plate capacitor equation and the values from table 4.1, where one conductor has potential and the other is grounded:

$$C_{ideal} = \varepsilon_0 \varepsilon_r \frac{S}{\delta_t} \approx 50pF \tag{4.5}$$

where

S : Surface of the conductors which faces adjacent conductors.
This is $h \cdot L = 1500\ mm^2$
δ_t : Interturn insulation thickness

The mutual capacitances can be found by equation 4.3 from the Maxwell capacitance matrix.

Turn-to-Ground Capacitance

Turn-to-ground capacitances are mainly determined by the distance and exposure to ground. As mentioned, if the t2g-capacitance is large compared to the mutual capacitances, the voltage distribution becomes uneven. The turn-to-ground capacitances can be found by equation 4.4 from the Maxwell capacitance matrix.

4 – Turn Winding

The equivalent circuit of the 4-turn winding is shown in figure 4.3. The notation "0" is devoted to ground. Each turn has at least one t2t-capacitance and one t2g-capacitance connected to its node.

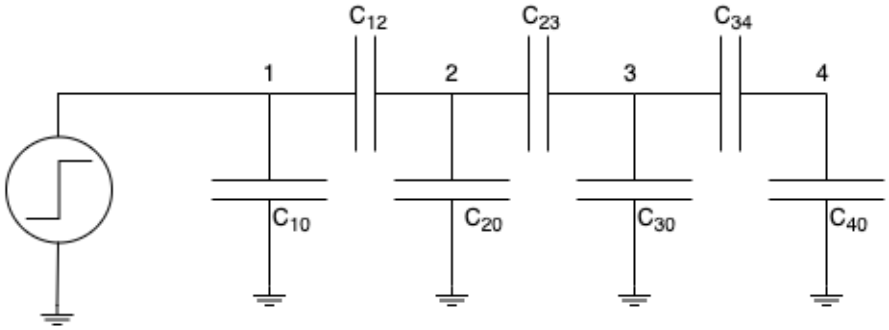

Figure 4.3: Equivalent circuit representation of the 4-turn winding

The resulting mutual capacitance matrix for the base case is given in $[pF]$ by the following matrix:

$$\mathbb{C}_{mutual} = \begin{bmatrix} 99.63 & 56.73 & 0.26 & 0.06 \\ 56.73 & 44.46 & 56.73 & 0.26 \\ 0.26 & 56.73 & 44.46 & 56.73 \\ 0.06 & 0.26 & 56.73 & 99.63 \end{bmatrix} \tag{4.6}$$

where the diagonal elements are the turn-to-ground capacitances and the non-diagonal the turn-to-turn capacitances. The t2t capacitances of matrix 4.6 are quite close to the ideal capacitance calculated in equation 4.5. The capacitances between non-adjacent turns are very low ($C < 1\ pF$), which is the reason they are neglected.

The same method of calculating capacitances is done in the parameter study, where parameters are changed one at a time in the 2D geometry, as shown in figure 4.2a. The resulting capacitance matrix is used to calculate the voltage distribution for each changing parameter.

8 – Turn Winding

Figure 4.4 shows the equivalent circuit of the 8-turn winding. Here, each turn has at least two t2t capacitances and one t2g capacitance connected to its node.

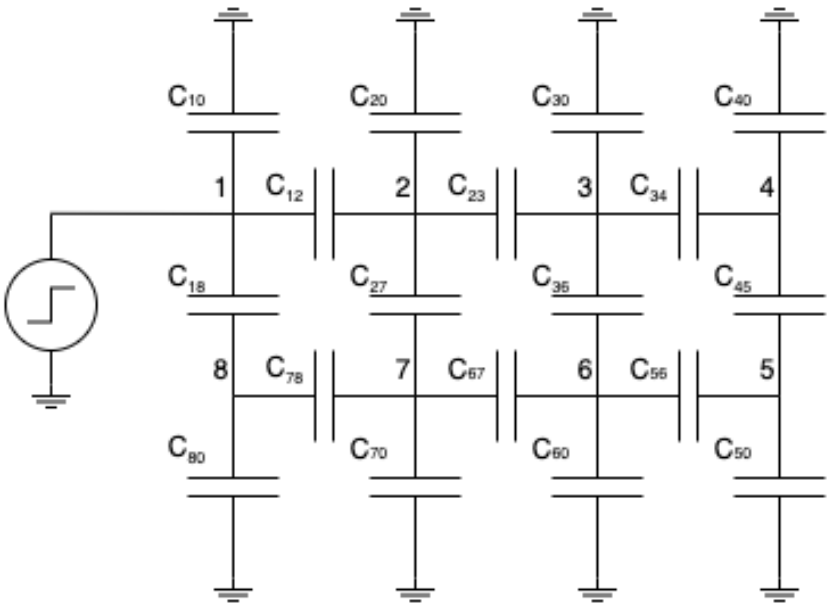

Figure 4.4: Equivalent circuit representation of the 8-turn winding

The mutual capacitance matrix 4.7 shows the calculated capacitances of the 8-turn winding, where the values are given in pF.

$$\mathbb{C}_{mutual} = \begin{bmatrix} 57.1 & 56.9 & - & - & - & - & - & 42.3 \\ 56.9 & 0.4 & 56.8 & - & - & - & 42.4 & - \\ - & 56.8 & 0.4 & 56.9 & - & 42.4 & - & - \\ - & - & 56.9 & 57.1 & 42.3 & - & - & - \\ - & - & - & 42.3 & 95.6 & 52.3 & - & - \\ - & - & 42.4 & - & 52.3 & 44.1 & 52.3 & - \\ - & 42.4 & - & - & - & 52.3 & 44.1 & 52.3 \\ 42.3 & - & - & - & - & - & 52.3 & 95.6 \end{bmatrix} \tag{4.7}$$

Only the mutual capacitances above 1 pF have been considered in this matrix since the capacitances of non-adjacent turns have low interference and thus can be neglected. The t2g-capacitance of turn 2 and 3 have remarkably lower value than the other turns. This is because they have the longest distance to ground. The effect of additional insulation in the interlayer has been studied, where additional thickness was added in the 2D geometry of the slot to calculate the resulting capacitance matrix, as shown in figure 4.2b.

4.2.3 Capacitive Voltage Distribution Calculation

The method of calculating the analytical voltage distribution is presented here. The pre-work presented an analytical formula to determine the voltage distribution. See

appendix A.2. However, this method is only applicable to chain configurations, which is a disadvantage. It does not apply to the 8-turn winding for instance. Because of this, the circuits were built in a circuit builder interface, where the calculated capacitances are inserted to find the resulting voltage distribution.

The electrical circuit interface in COMSOL Multiphysics®was used here, where the circuits in figure 4.3 and 4.4 are built by defining the connection nodes and the component values. By applying a voltage to the circuits, an electrostatic voltage distribution is obtained.

4.3 Finite Element Method

There are several reasons to use FEM in research and development of new technology. Towards AEA, every component will have to evolve and mature the next decades to reach the levels of power density needed. The methodology of the finite element method will now be presented.

4.3.1 Computational Electromagnetics

One of the starting points in building any FEM model is to select the physics needed. Usually, this is straight forward since most of the electrical modules solve Maxwell's equations. However, the most used feature is based on the quasi-static regime, which considers the electric field to be in-variant. Thus, the RF module is chosen as physics in the selected FEM software, due to its applicability to high frequent and non-linear systems.

Another important aspect is the electrical size, which is the ratio of the maximum dimension of the object analyzed L_c and the wavelength λ [31]. The wavelength is the ratio between the velocity and operating frequency, as shown by the following:

$$\lambda = \frac{v}{f_e} \tag{4.8}$$

where the velocity is determined by the permittivity of the dielectricum, as shown in eq.3.2. The maximum characteristic frequency associated with the voltage input signal can be found analytically by the inverse of the minimum rise time [32].

$$f_e \approx \frac{1}{t_r} \tag{4.9}$$

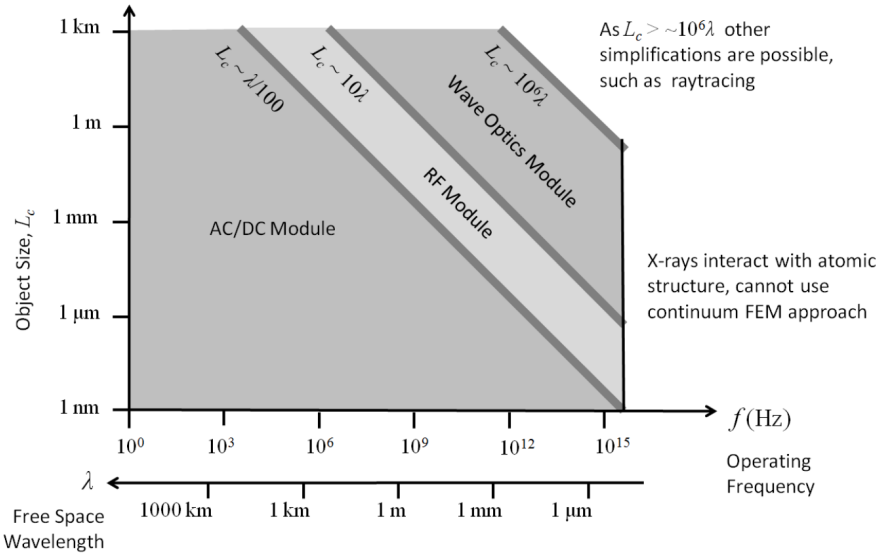

Figure 4.5: Range applicability of the AC/DC, RF and Wave Optics modules in COMSOL Multiphysics®[31]

Figure 4.5 shows the applicability of different modules in the chosen FEM-software, where the AC/DC module dominates in most electrical analysis.

The maximum dimension of the windings used in this thesis is considered the slot length, which is 0.3 m, see table 4.1. The maximum characteristic frequency is approximately 166.67 MHz by equation 4.9 and the rise time from figure 4.11. The electrical size then yields:

$$\frac{L_c}{\lambda} = \frac{0.3m}{\frac{c}{\sqrt{3}} \cdot 6ns} \approx 1 \tag{4.10}$$

where, c is the speed of light in vacuum. Hence, the maximum electrical size of the object is approximately equal the wavelength, $L_c \sim \lambda$.

4.3.2 Modelling Constraints

When using FEM-software, a variety of choices have to be taken to simplify certain areas of the model. By simplifying geometry, such as replacing volumetric domains with boundary conditions where it is possible, can reduce the memory and computational power required to solve the solutions. This applies mostly for 3D models.

Conductor Domain

The conductor used in this thesis is rectangular copper wires, due to its advantage with improved fill factor. In practice, litz would have been preferred due to its applicability in high-frequency ranges with reduced losses, skin- and proximity effects. Anyhow, due to its complex structure, it is difficult to build and simulate in FEM.

Either way, the copper domain is omitted from the model. One of the reasons for this is that a rectangular copper conductor will be subjected to skin effect. Due to the high frequency, the skin depth will be very thin. Hence, the current density will exist at the circumference of the copper wire only. The interior boundaries of the conductor domain are kept, such that the boundaries can be defined with a lossless boundary condition able to conduct ideally [33]. Moreover, by omitting the conductor domain from the model decreases the number of elements in the model, which decreases the computational demand.

Insulation Domain

The turn and mainwall insulation are merged to minimize the number of elements. By merging these, the elements created are allowed to be larger, which can at least halve the number of elements. The figure below shows the transition from the turn- and mainwall insulation separated to merged for the 8-turn winding.

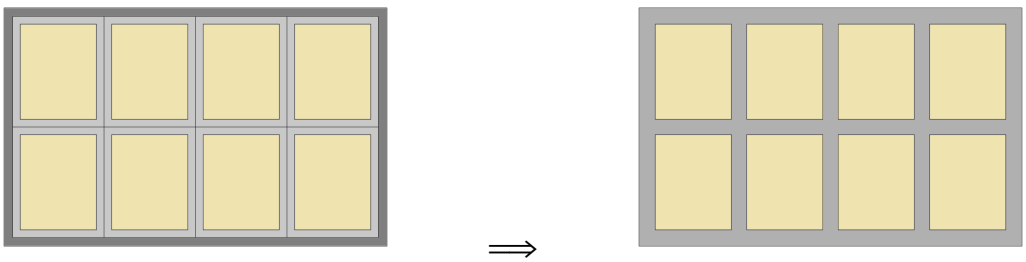

(a) Turn and mainwall insulation separated

(c) Turn and mainwall insulation merged

Transposition

The 8-turn winding consists of two 4-turn layers on top of each other wound oppositely. A transposition is therefore needed. The transposition is the trickiest geometry built in this thesis. It is placed in the close side overhang to save slot space. Figure 4.7 shows the actual transposition of the 8-turn winding, which connects turn 4 and 5.

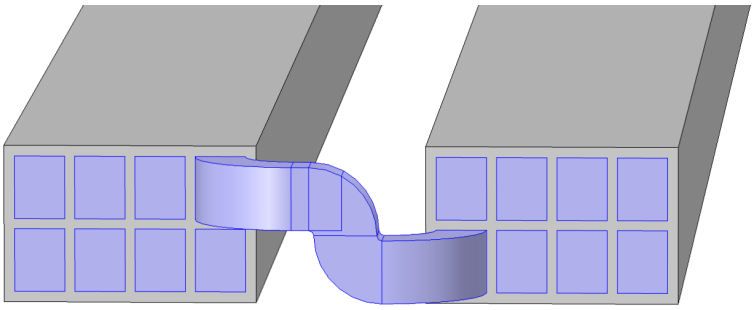

Figure 4.7: Transposition of 8 turn coil

Materials

The materials used in the modelling have no other purposes than to define the relative permittivity. The turn and mainwall insulation are equal from the base case in table 4.1. Thus, mica has been used with $\varepsilon_r = 3$ in both. The disadvantage with having the turn and mainwall insulation merged, is that they cannot have different permittivities.

The copper domain is omitted from the model and will therefore not need to be defined with a material. The remaining, which is the outer box surrounding the winding, is defined as air. Figure 4.8 illustrates the outer box and the 8-turn winding within.

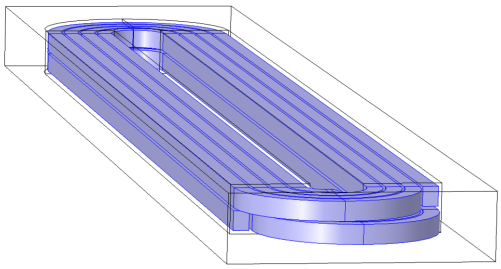

Figure 4.8: Outer air box which encapsules the 8-turn winding

4.3.3 Electromagnetic Waves, Transient

Transient electromagnetic waves (TEMW) is the interface within the selected physics used to simulate the voltage distribution. This interface solves time-domain wave equations for the magnetic vector potential and is well suited for non-linear electromagnetic behaviour and time-domain reflectometry.

Wave Equation, Electric

The wave equation solved for in the TEMW interface is given in the user's guide [34]. The equation is not used directly in this thesis, but rather to show which variables and inputs that determine the outcome. In a transient time domain, the Maxwell-Ampere's equation (A.8) can be derived further by using the relations to magnetic potential:

$$\mu \boldsymbol{H} = \nabla \times \boldsymbol{A} \tag{4.11}$$

$$\boldsymbol{E} = -\frac{\partial \boldsymbol{A}}{\partial t} \tag{4.12}$$

The time-varying wave equation calculated in the TEMW interface can then be found:

$$\nabla \times \mu_r^{-1}(\nabla \times \boldsymbol{A}) + \mu_0 \sigma \frac{\partial \boldsymbol{A}}{\partial t} + \mu_0 \frac{\partial}{\partial t}(\varepsilon \frac{\partial \boldsymbol{A}}{\partial t}) = 0 \tag{4.13}$$

This equation solves for the magnetic vector potential, where the other inputs are the relative permittivity ε_r, relative permeability μ_r and the electrical conductivity σ. The equation can alternatively be rewritten by using the relation $\varepsilon_r = n^2$, which gives:

$$\mu_0 \varepsilon_0 \frac{\partial}{\partial t}(n^2 \frac{\partial \boldsymbol{A}}{\partial t} + \nabla \times (\nabla \times \boldsymbol{A}) = 0 \tag{4.14}$$

where n is the refractive index [34].

Perfect Electric Conductor

The perfect electric conductor (PEC) is a surface representing an idealized (lossless) electric conductor. It is a particular case of the electric field boundary condition that sets the tangential component of the electric field to zero [34]. In fact, due to no losses, the PEC boundary condition will reflect any incident wave 100 % [35]. This boundary can be used on highly conductive mediums and/or lossless metallic surfaces, such as ground plane or as a symmetry type boundary condition [34]. It imposes symmetry for magnetic fields and currents, and antisymmetry for electric fields and currents. The equation solved for in PEC is the following:

$$\boldsymbol{n} \times \boldsymbol{E} = 0 \tag{4.15}$$

The PEC boundary is used to represent the surfaces of the conductor in the winding models. As mentioned, the current density is only flowing at the circumference of the rectangular copper wire due to the skin effect. Thus, the PEC boundary condition is placed at surfaces of interior boundaries of the conductor. Additionally, PEC is used to define ground plane.

Lumped Port

The lumped port is used to apply a voltage or current excitation to a model or to connect an external circuit. The lumped port can only be used on a boundary that extends between to metallic boundaries, meaning boundaries where PEC or Impedance boundary conditions are applied [34]. Additionally, the distance between these two metallic boundaries must be much smaller than the wavelength, so that a local quasi-static approximation is justified [36].

The lumped port provides an interface between electric- and magnetic fields, and voltages and currents. The gap must be much less than the wavelength to define the electric field from voltage. This is to justify the requirement on lumped port; the feed point must be similar to a transmission line feed [34]. The relation between voltage and electric field can then be determined by:

$$V = \int_h (\boldsymbol{E} \cdot \boldsymbol{a}_h) dl \tag{4.16}$$

where $\boldsymbol{a}_h$ is a vector element determining the direction of the electric field. Figure 4.9 shows the feed point of the transmission line where lumped port is used. The electric

field is integrated along h, which is the height of the gap between positive phase V and ground.

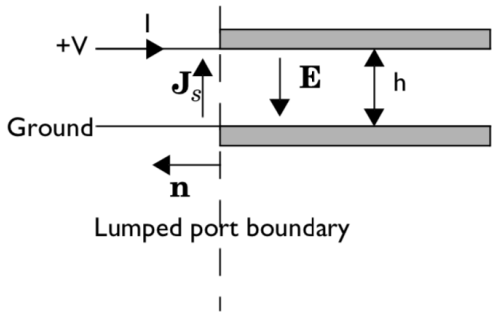

Figure 4.9: Lumped port description of parameters [34]

The transmission line impedance is defined by

$$Z = \frac{V}{I} \tag{4.17}$$

which can be used to define an equivalent surface impedance at the lumped port boundary in:

$$\eta = \frac{\boldsymbol{E} \cdot \boldsymbol{a}_h}{\boldsymbol{J}_s \cdot (-\boldsymbol{a}_h)} \tag{4.18}$$

The current can be calculated from the surface current density by integrating along the width, w, of the lumped port boundary:

$$I = \int_w (\boldsymbol{n} \times \boldsymbol{J}_s)\boldsymbol{dl} = -\int_w (\boldsymbol{J}_s \cdot \boldsymbol{a}_h)dl \tag{4.19}$$

where the integration is taken in the direction of $\boldsymbol{a}_h \times \boldsymbol{n}$. The relation between the transmission line impedance and surface impedance can then be found by implementing equation 4.16 and 4.19 into equation 4.17:

$$Z = \frac{V}{I} = \frac{\int_h (\boldsymbol{E} \cdot \boldsymbol{a}_h)dl}{-\int_w (\boldsymbol{J}_s \cdot \boldsymbol{a}_h)dl}$$

which can be rewritten further by the use of equation 4.18:

$$Z = \eta \frac{\int_h (\boldsymbol{E} \cdot \boldsymbol{a}_h)dl}{\int_w (\boldsymbol{E} \cdot \boldsymbol{a}_h)dl} \approx \eta \frac{h}{w} \tag{4.20}$$

The approximation here is done under the assumption that the electric field is constant over the integrations.
Equation 4.20 is a transfer equation used in an impedance type boundary condition, which relates the surface current density to the tangential electric field via the surface impedance. The total field at the lumped port can be found in the following equation:

$$\boldsymbol{n} \times (\boldsymbol{H}_1 - \boldsymbol{H}_2) + \frac{1}{\eta}\boldsymbol{n} \times (\boldsymbol{E} \times \boldsymbol{n}) = 2\frac{1}{\eta}\boldsymbol{n} \times (\boldsymbol{E}_0 \times \boldsymbol{n}) \tag{4.21}$$

where $\boldsymbol{E}$ is the total electric field and $\boldsymbol{E}_0$ is the incident field, which corresponds via equation 4.16 to total voltage V and incident voltage V_0. It is the incident voltage that is the input signal at

There are several terminal types which can be selected at the lumped port boundary, such as current driven port, cable driven port or circuit port. For this model, both the cable and circuit terminal types have been considered. Due to simplicity reasons, circuit port has been used to connect an external circuit to the 3D model.

4.3.4 Electrical Circuit

The external circuit applies a voltage excitation to the 3D model, as illustrated in figure 4.10. The electrical circuit is connected via a unique feature: External I vs. U, which is a feature that connects an arbitrary voltage measurement, such as the lumped port boundary, as a voltage source between two nodes in the electrical circuit [34].

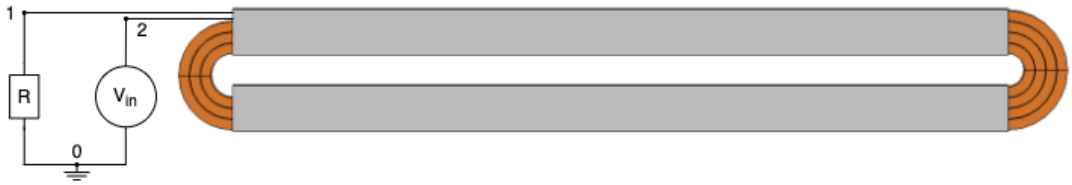

Figure 4.10: External circuit connection

The voltage source excites the port boundary of the FEM model with the input signal. A step signal with a short rise time is chosen to provoke the transient effects in the windings. The input signal is shown in figure 4.11, where the signal goes from 0 - 100 % in 10 ns. Because of the different switching patterns at the beginning and end of different switching devices, the rise time is generally defined as the time required of a signal to rise from 10 % to 90 % of its stationary value. By definition, this gives a rise time $t_r = 6\ ns$.

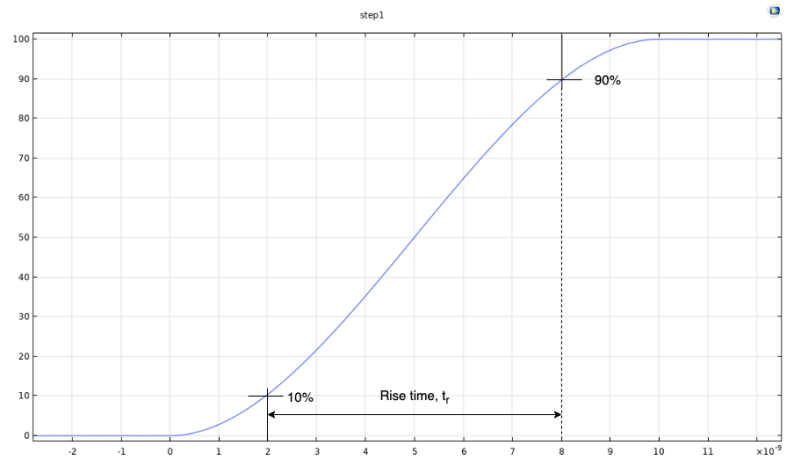

Figure 4.11: Input signal from the voltage source with the definition of rise time included

4.3.5 Mesh

Finite element method creates a mesh containing several elements, whereas the solution is approximated within each element. As specified, the number of elements mainly determines the computational size of the object. The windings studied have a considerable difference between the maximum and minimum dimensions, whereas the maximum dimension is the length of the airbox and the minimum insulation thickness between turns.

There are no specific blueprints to a mesh that has good quality since each study has different requirements. A general rule of thumb is stated, however; the mesh elements are considered poor if the quality is below 0.1 [37]. An attempt to achieve minimum element quality above 0.1 was done by sweeping the interturn insulation and adding several meshes with different sizes. Both attempts ended in heavily computational demands, where the result did not seem to change significantly. By using the physics-controlled mesh, the computational demand was not nearly as high as for the other two, although the result was much the same.

The physics-controlled mesh conjures a parameter for the maximum element mesh size in free space, which it automatically scales with the wavelength from different dielectric and magnetic regions [34]. The default setting is used, which defines the maximum element mesh size as 1/5 of the wavelength from the highest frequency.

4.3.6 Post – Processing

To extract the voltages between turns and turn to ground, the electric field has to be integrated. Lines from each turn to ground and between adjacent turns are drawn in the geometry to be integrated over.

Chapter 5

Results

This chapter presents the analytical and FEM results, followed by a comparison of the two methods. The results are divided into three sections. First, the analytical results of the 4-turn and 8-turn winding are presented. Then, similarly, the FEM results are presented. Lastly, the comparison of the two study methods, which also are divided by the winding configuration.

5.1 Analytical Results

5.1.1 4 – Turn Winding

This section presents the resulting voltage distribution of the base case and parameter study of the 4-turn winding. The base case of the 4-turn winding will be the reference to the parameter studies, where one parameter is adjusted at a time while the others remain fixed. The effect each parameter has on the voltage distribution will be measured by comparing the resulting distribution to the reference.

Base Case

The resulting voltage distribution of the base case is tabulated in table 5.1, where t2g- and t2t-voltages are shown. It can be seen that almost 60 % of the input voltage appeared over the first two turns.

Table 5.1: Voltage distribution of the 4-Turn model [%]

V_{10}	V_{20}	V_{30}	V_{40}	V_{12}	V_{23}	V_{34}
100	41.2	14.8	0	58.8	26.4	14.8

5.1.2 Parameter Study

The parametric study presented here is done to see how some parameters affect the t2t- and t2g-capacitances, and the ratio between them, which determines the voltage

distribution. Parameters such as turn- and mainwall insulation thickness, permittivity and different grounding have been examined. The parameters have been examined one at a time, with values below and above the base dimensions of table 4.1. Additionally, a special case where additional turn insulation at first turn only has been studied.

Grounding

Six different grounding cases have been studied to see how they affect the capacitances and the voltage distribution. Figure 5.1 – 5.6 illustrate the different grounding cases, where a blue line marks the boundary condition where ground is placed.

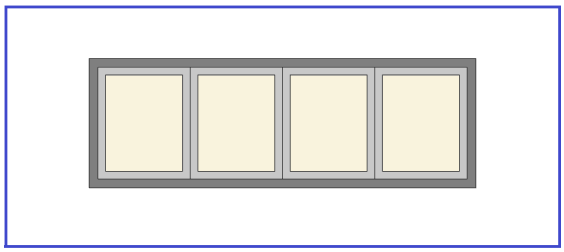

Figure 5.1: Grounding Case A

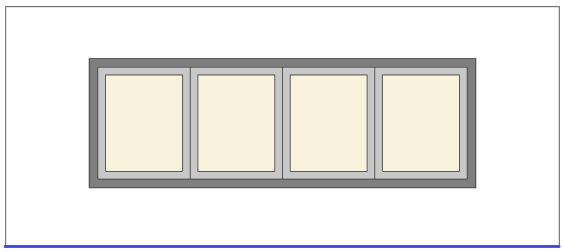

Figure 5.2: Grounding Case B

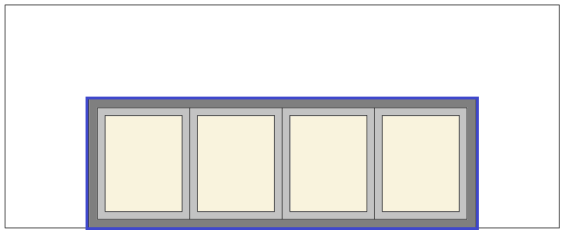

Figure 5.3: Grounding Case C

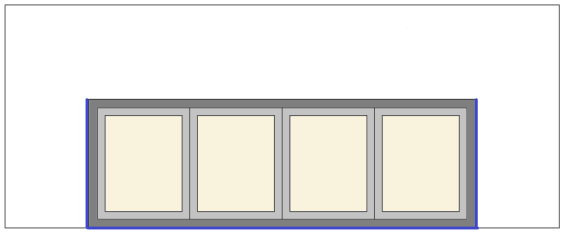

Figure 5.4: Grounding Case D

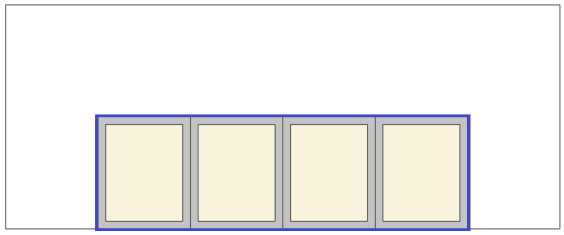

Figure 5.5: Grounding Case E

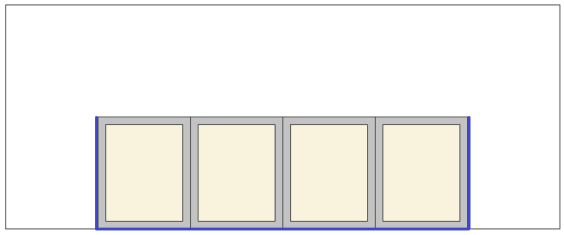

Figure 5.6: Grounding Case F

The colour represents:

Blue: Ground boundaries
Beige: Conductors
Dark grey: Mainwall insulation
Light grey: Turn insulation
White: Surrounding air

The first two cases represent an air winding, where the winding is insulated by turn and mainwall insulation. Case A has ground condition along the circumference of the outer air boundaries, while case B has ground at the lower boundary only. These two

cases can, in some way, represent the overhang section of a winding since that section is not directly exposed to ground.

Case C and D represent the same winding as case A and B, but with the grounding more similar to a winding in a stator slot. Case C has ground condition along the circumference of the mainwall insulation, while case D has an open top. Case D represents the base case grounding.

Lastly, case E and F represent a winding with turn insulation only, where case F has ground along the outer circumference of the winding, while case F has an open top. Although case E and F are unrealistic due to no main insulation, the effect of ground on such close hold can be examined.

The t2g- and t2t-capacitances in these cases are shown in table 5.2. The t2g-capacitances have the most significant changes by relocating ground, while the t2t-capacitances can be seen to have minor changes. The changing t2g-capacitance will thus determine the C_g/C_t-ratio. The ratio was largest in case E and F, which would result in the worst distribution amongst these cases, analytically.

Table 5.2: Capacitance result of the different ground cases

Cases	$C_{10}, C_{40}\ [pF]$	$C_{20}, C_{30}\ [pF]$	$C_{t2t}\ [pF]$	C_g/C_t
Case A	16	9.3	59.2	2.71
Case B	7.25	4.6	60.4	1.2
Case C	138	88.1	52.2	2.64
Case D	99.6	44.5	56.7	1.76
Case E	281	184	48.9	5.76
Case F	199	92.2	54	3.68

The resulting voltage distribution can be seen in table 5.3. Case B appears with close to even distribution, while case E has the worst distribution where 82.1 % of the input voltage appears over the first two turns.

Table 5.3: Capacitive distribution different grounding cases

Cases:	V_{10}	V_{20}	V_{30}	V_{40}	V_{12}	V_{23}	V_{34}
Case A	100	59.0	27.4	0	41	31.7	27.4
Case B	100	62.7	30.2	0	37.3	32.5	30.2
Case C	100	29.3	7.9	0	70.7	21.3	7.9
Case D	100	41.2	14.8	0	58.8	26.4	14.8
Case E	100	17.9	3.1	0	82.1	14.8	3.1
Case F	100	29.1	7.8	0	70.9	21.2	7.8

Turn Insulation Thickness

The interturn insulation thickness δ_t is examined for five different values, from 0.2 mm to 1.0 mm, with an increment of 0.2 mm. The resulting capacitances are tabulated in table 5.4.

Table 5.4: Capacitance result of different interturn insulation thickness

δ_t $[mm]$:	C_{10}, C_{40} $[pF]$	C_{20}, C_{30} $[pF]$	C_{t2t} $[pF]$	C_g/C_t
0.2	144	61	211	0.68
0.4	125	54	109	1.14
0.6	110	48.6	74.3	1.49
0.8	99.6	44.5	56.7	1.76
1.0	91	41.2	46.1	1.97

The results are in agreement with equation 4.5, whereas an increase of insulation thickness between turns decreases the t2t-capacitance. Thicker turn insulation will also increase the distance from ground, which results in lower values of t2g-capacitances. However, this difference has little significance compared to t2t-capacitances. Thus, C_g/C_t ratio decreases with thinner insulation due to the difference in t2t-capacitance.

Table 5.5 presents the resulting distribution from the different turn insulation thicknesses. The distribution is worst for 1 mm insulation thickness.

Table 5.5: Capacitive voltage distribution for different turn insulation thickness

	Voltages $[V]$						
δ_t $[mm]$:	V_{10}	V_{20}	V_{30}	V_{40}	V_{12}	V_{23}	V_{34}
0.2	100.0	54.0	23.6	0	46.0	30.4	23.6
0.4	100.0	47.8	19.1	0	52.2	28.6	19.1
0.6	100.0	43.9	16.5	0	56.1	27.4	16.49
0.8	100.0	41.2	14.8	0	58.8	26.4	14.8
1.0	100.0	39.2	13.6	0	60.8	25.7	13.6

Additionally, more layers of turn insulation around the first turn only has been studied. Table 5.6 contains the capacitance values from this study. Only C_{10} and C_{12} had noticeable changes, where both became lower with additional layers. C_{10} and C_{12} determine the C_g/C_t-ratios here.

Table 5.6: Capacitance result of additional turn insulation at first turn

δ_{t1}	Capacitances $[pF]$					
$[mm]$	C_{10}	C_{20}, C_{30}	C_{40}	C_{12}	C_{t2t}	C_g/C_t
0.1	90.7	44.6	99.7	50.7	56.9	1.97
0.2	83.7	44.8	99.7	45.9	56.9	2.17
0.3	77.9	45.1	99.7	42.0	56.9	2.38
0.4	73.1	45.3	99.7	38.8	56.9	2.58

By adding more turn insulation layers, the capacitive voltage distribution becomes more uneven, as shown in table 5.7

Table 5.7: Voltage distribution for additional turn insulation at first turn

	Voltages $[V]$						
δ_{t1} $[mm]$:	V_{10}	V_{20}	V_{30}	V_{40}	V_{12}	V_{23}	V_{34}
0.1	100	38.5	13.8	0	61.5	24.6	13.8
0.2	100	36.1	13.0	0	63.9	23.2	13.0
0.3	100	34.0	12.2	0	66.0	21.8	12.2
0.4	100	32.2	11.6	0	67.8	20.7	11.6

Mainwall Insulation Thickness

The mainwall insulation thickness is varied from 0.25 mm to 0.65 mm, with an increment of 0.10 mm. By having a thicker or thinner mainwall thickness, the distance from ground will increase or decrease, which will decrease or increase the t2g-capacitances, respectively. The t2t-capacitance has insignificant changes. The C_g/C_t-ratio will, therefore, increase with a thinner mainwall insulation thickness, and decrease when the distance to ground becomes more significant by a thicker mainwall insulation. See table 5.8.

Table 5.8: Capacitance result of different mainwall insulation thickness

δ_m $[mm]$:	C_{10}, C_{40} $[pF]$	C_{20}, C_{30} $[pF]$	C_{t2t} $[pF]$	C_g/C_t
0.25	126	57.6	55.5	2.28
0.35	111	50.2	56.2	1.98
0.45	99.6	44.5	56.7	1.76
0.55	90.4	39.9	57.2	1.58
0.65	82.8	36.2	57.6	1.44

Table 5.9 shows the voltage distribution for the different mainwall thicknesses. By having a thinner mainwall, the distribution becomes more uneven. By having a mainwall insulation thickness of 0.25 mm, 63.1 % of the input voltage is distributed over the first two turns.

Table 5.9: Capacitvie voltage distribution different mainwall insulation thickness

	Voltages $[V]$						
$\delta_m\ [mm]$:	V_{10}	V_{20}	V_{30}	V_{40}	V_{12}	V_{23}	V_{34}
0.25	100.0	36.9	12.2	0.0	63.1	24.8	12.2
0.35	100.0	39.3	13.6	0.0	60.7	25.7	13.6
0.45	100.0	41.2	14.8	0.0	58.8	26.4	14.8
0.55	100.0	43.0	15.9	0.0	57.0	27.0	15.9
0.65	100.0	44.5	16.9	0.0	55.5	27.6	16.9

Turn Insulation Permittivity

Here, the turn insulation permittivity $\varepsilon_{r,turn}$ is varied. The mainwall insulation permittivity is fixed at the base value $\varepsilon_r = 3$, see table 4.1.

Table 5.10: Capacitance result of different turn insulation permittivities

$\varepsilon_{r,turn}$	$C_{10}, C_{40}\ [pF]$	$C_{20}, C_{30}\ [pF]$	$C_{t2t}\ [pF]$	C_g/C_t
2	66.9	29.8	38.1	1.76
3	99.6	44.5	56.7	1.76
4	132	59.1	75.3	1.76
5	165	73.8	93.9	1.76
6	198	88.5	113	1.76

The $\varepsilon_{r,turn}$ affects the t2g- and t2t-capacitances equally, which results in the same C_g/C_t-ratio for all cases, see table 5.10.
The changing permittivity in turn insulation had no changes in voltage distribution due to equal C_g/C_t-ratio. All were equal the base case voltage distribution shown in table 5.1.

Mainwall Insulation Permittivity

Now, the relative permittivity of the mainwall insulation is analyzed. $\varepsilon_{r,mainwall}$ is varied from 2 – 6, with an increment of 1, where $\varepsilon_{r,turn}$ is fixed at $\varepsilon_r = 3$.

Table 5.11: Capacitance result of different mainwall insulation permittivities

$\varepsilon_{r,mainwall}$	$C_{10}, C_{40}\ [pF]$	$C_{20}, C_{30}\ [pF]$	$C_{t2t}\ [pF]$	C_g/C_t
2	79.7	35.4	56.6	1.41
3	99.6	44.5	56.7	1.76
4	114	51	56.9	2.01
5	125	56	57.1	2.19
6	134	60	57.3	2.34

The t2g-capacitances increases with increasing $\varepsilon_{r,mainwall}$, see table 5.11. However, the t2t-capacitance has minor changes, which affects the ratio to be determined by C_g mainly. In table 5.12, the voltage over the first two turns, V_{12}, became higher with increasing $\varepsilon_{r,mainwall}$.

Table 5.12: Capacitive voltage distribution from different mainwall permittivities

	Voltages $[V]$						
$\varepsilon_{r,mainwall}$	V_{10}	V_{20}	V_{30}	V_{40}	V_{12}	V_{23}	V_{34}
2	100.0	44.6	17.0	0.0	55.4	27.6	17.0
3	100.0	41.2	14.8	0.0	58.8	26.4	14.8
4	100.0	39.2	13.5	0.0	60.8	25.7	13.5
5	100.0	37.8	12.7	0.0	62.2	25.1	12.7
6	100.0	36.8	12.1	0.0	63.2	24.7	12.1

5.1.3 8 – Turn Winding

Analytical results of the 8-turn winding are presented here. The findings from the parametric study of the 4-turn winding generally apply in the same manner for the 8-turn winding. Nevertheless, the effect of additional insulation between the two layers has been examined to see how it affects the capacitive voltage distribution.

Throughout the study of this configuration, four cases have been investigated with respect to voltage distribution, all of them with base dimensions from table 4.1:

T1 - represents the case where voltage input is at turn 1 and turn 8 grounded.
T1o - represents the case where voltage input is at turn 1 and turn 8 open.
T8 - represents the case where voltage input is at turn 8 and turn 1 grounded.
T8o - represents the case where voltage input is at turn 8 and turn 1 open.

Base Case

The voltage distribution from these cases are given in table 5.13 and 5.14, which shows the t2g- and t2t voltages, respectively.

Table 5.13: Turn-to-ground voltages for voltage input at turn 1 and turn 8

V_{input}	Turn-to-ground voltages $[V]$							
	V_{10}	V_{20}	V_{30}	V_{40}	V_{50}	V_{60}	V_{70}	V_{80}
T1	100	48.9	24.4	10.3	5.2	10.6	13.7	0
T1*o*	100	52.6	27.2	11.7	6.5	14.2	23.4	28.7
T8	0	12.6	9.7	4.8	4.5	12.6	33.6	100
T8*o*	38.5	31.5	19.1	8.7	6.5	16.7	38.9	100

Figure 5.7a and 5.7b illustrate the voltage distributed across turns in all cases. It can be seen from both figures that there is almost no difference between open and grounded end for the first four turns, whereas the first turn is referred to the turn connected to voltage input. The last four turns, however, set the difference. Both T8 cases can be seen to have more significant drops over the first turns, than the T1 cases.

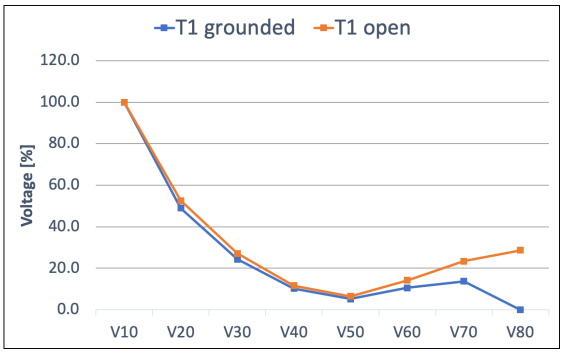

(a) T1 - t2g voltage distribution for open and grounded end

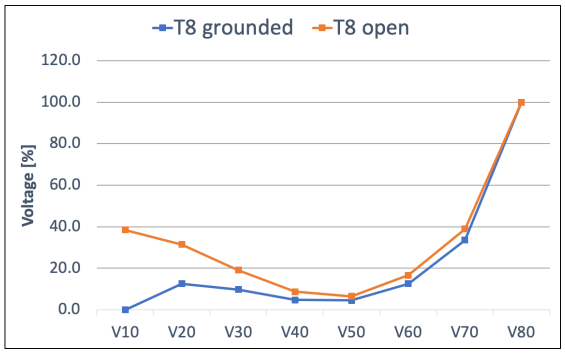

(b) T8 - t2g voltage distribution of open and grounded end

Figure 5.7: Turn-to-ground voltage distribution of T1 and T8

Table 5.14 shows the voltage distribution between adjacent turns. This is represented in such way that $V_{xy} = V_x$ - V_y.

Table 5.14: Turn-to-turn voltages for voltage input at turn 1 and turn 8

V_{in}	Turn-to-turn voltages $[V]$									
	V_{12}	V_{23}	V_{34}	V_{45}	V_{56}	V_{67}	V_{78}	V_{18}	V_{27}	V_{36}
T1	51	24.5	14.1	5.1	-5.4	-3.1	13.7	100	35.2	13.8
T1*o*	47.4	25.4	15.5	5.2	-7.7	-9.2	-5.3	71.3	29.2	13
T8	-12.6	2.9	5	0.2	-8.1	-21	-66.4	-100	-21	-2.9
T8*o*	7.0	12.4	10.4	2.2	-10.2	-22.2	-61.1	-61.5	-7.4	2.4

Considering T1 and T1o first, it can be seen that by grounding the last turn, 100 % of the incident voltage appear between the first and last turn. The turns furthest away from the input have the lowest voltages, such as V_{45}, V_{56} and V_{67}. By having the last turn open, the voltage over the first and last turn reduces to 71 %. Generally, the highest voltages are reduced and the lowest are increased by having an open end. T1 has a higher distribution over the vertically adjacent turns regardless open or grounded end, compared to T8.

T8 and T8o can be seen to have highest voltage over the turns adjacent to the input turn as well, such as V_{78} and V_{18}. The voltage distribution in T8 and T8o appear worse than in T1 and T1o, although V_{18} is lower in T8o than T1o. T8o resulted in close to equal voltage over V_{18} and V_{78}, which is interesting since all others had the highest voltage over V_{18}. Similarly to T1 and T1o, by going from grounded to open last turn, the highest voltages are reduced and the lowest are increased.

Interlayer Insulation Thickness

Two different cases of interlayer insulation thickness has been studied. The thicknesses studied are 0.1 and 0.2 mm. The resulting capacitances is shown in table 5.15.

Table 5.15: Capacitance values from different additional insulation layer between upper and lower deck

$\delta_i\ [mm]$	Capacitance $[pF]$						
	C_{10}, C_{40}	C_{20}, C_{30}	C_{50}, C_{80}	C_{60}, C_{70}	$C_{t2t,upper}$	$C_{t2t,lower}$	$C_{t2t,mid}$
0.0	57.1	0.39	95.6	44.1	56.9	52.3	42.3
0.1	57.3	0.40	95.9	44.1	57.0	52.4	37.1
0.2	57.7	0.39	96.2	44.1	57.2	52.6	33.1

An increment of 0.1 mm is arguably very small to see a large difference. The result from table 5.15 reflects that the only noticeable difference was the t2t-capacitances between layers, which makes sense. Thicker insulation results in a lower t2t-capacitance.

Table 5.16: Turn-to-turn voltages for T1, T1o, T8 and T8o with additional interlayer insulation

Case	δ_i	Turn-to-turn voltages $[V]$									
	$[mm]$	V_{12}	V_{23}	V_{34}	V_{45}	V_{56}	V_{67}	V_{78}	V_{18}	V_{27}	V_{36}
T1	0.1	49.6	24.9	14.7	5.8	-5.1	-2.8	12.9	100	37.5	15.4
	0.2	48.3	25.1	15.2	6.5	-4.9	-2.4	12.2	100	39.5	16.8
T1o	0.1	46.5	25.5	15.9	5.8	-7.3	-8.4	-4.3	73.8	31.6	14.5
	0.2	45.6	25.7	16.3	6.5	-6.9	-7.7	-3.6	75.9	33.8	15.9
T8	0.1	-11.9	2.5	4.7	0.1	-8.2	-21.4	-65.9	-100	-22.3	-3.4
	0.2	-11.2	2.2	4.5	0.1	-8.4	-21.7	-65.4	-100	-23.4	-4.0
T8o	0.1	5.9	11.4	10	2.2	-10	-22.4	-61.3	-64.3	-8.9	2
	0.2	4.9	10.6	9.5	2.1	-10	-22.5	-61.4	-66.6	-10.2	1.7

From the voltage distribution in table 5.16, it can be seen that the small increase in thickness had minor changes in voltage between turns. Most substantial differences were, not surprisingly, over the capacitances between the upper and lower layer.

5.2 FEM Simulations

5.2.1 4 – Turn Winding

The FEM simulations of the 4-turn winding are presented here. Figure 5.9 shows the areas of the winding where measurements have been done. Both overhang-segments, both left and right slot at the input side and both left and right mid-slot have been considered for the base case. Turn-to-ground measurements have been extracted from the left and right slot only. Turn-to-turn measurements have been done in all areas. The left and right slot can also be referred to as the start and end of each turn. The voltage input is located at the start of turn 1 and ground at the end of turn 4, as shown in figure 5.8.

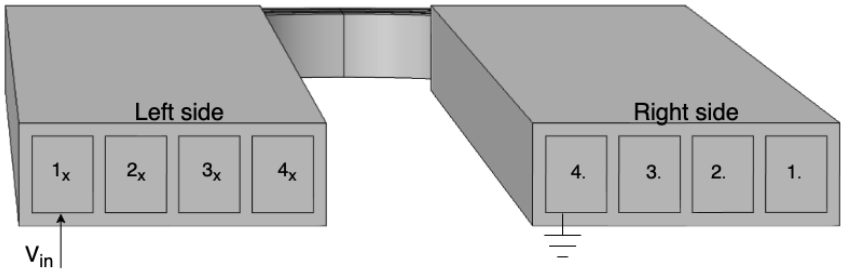

Figure 5.8: Slot explaination of the 4 turn winding

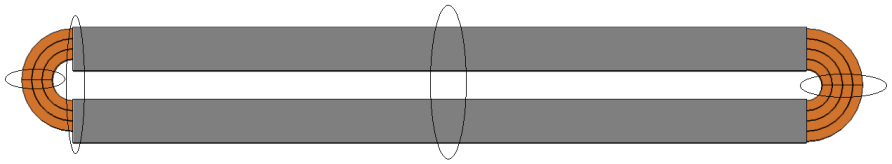

Figure 5.9: Measuring points in the 3D winding model

Turn-to-Ground Measurements

The turn-to-ground measurements are extracted from both slots, as shown by figure 5.10a and 5.10b. The oscillations in the winding are quite large, which indicate a high ringing effect. This can be due to the PEC which reflects the waves 100 % in addition to a grounded last turn. It can be seen that V_{10}, V_{20} and V_{30} in figure 5.10b are similar to V_{20}, V_{30} and V_{40} of figure 5.10a, respectively. The abbreviation, LCS and RCS refer to the left- and right close-side, respectively, as expressed in figure 5.8.

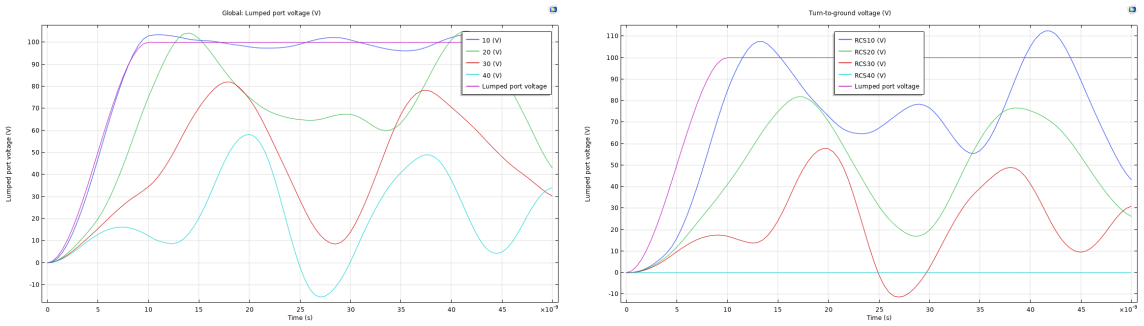

(a) Left slot (Input) **(b)** Right slot (ground)

Figure 5.10: Turn-to-ground voltages

Turn-to-Turn Measurements

In the left slot, the t2t-voltage appears highest between turn 2 and 3, after a few oscillations. The peak is approximately 58 V, see figure 5.11a. Figure 5.11b shows the grounded side, where the voltage between turn 1 and 2 reach the highest peak of approximately 62 V. Additionally, RCS12 and RCS34 can be seen to have similar peak-to-peak voltage.

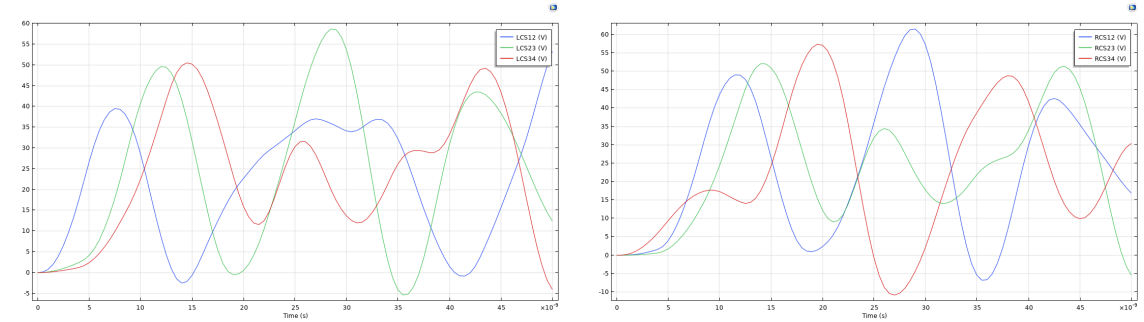

(a) Left slot (voltage input) **(b)** Right slot (grounded)

Figure 5.11: Turn-to-turn voltages in the left and right slot

Figure 5.12 display the turn-to-turn voltage simulations in the mid-slot. The left mid-slot (LMS) simulations in figure 5.12a have lower peak values than the input side in figure 5.11a. Also, the peak-to-peak voltage between turn 2 and 3 is highest in the left mid-slot, while the peak-to-peak voltage between turn 1 and 2 is highest in the right mid-slot. Similarly, the right mid-slot (RMS) plot in figure 5.12b can be seen to have slightly lower peak values than figure 5.11b. However, V_{23} has a higher peak in the right mid-slot than in the right close-side.

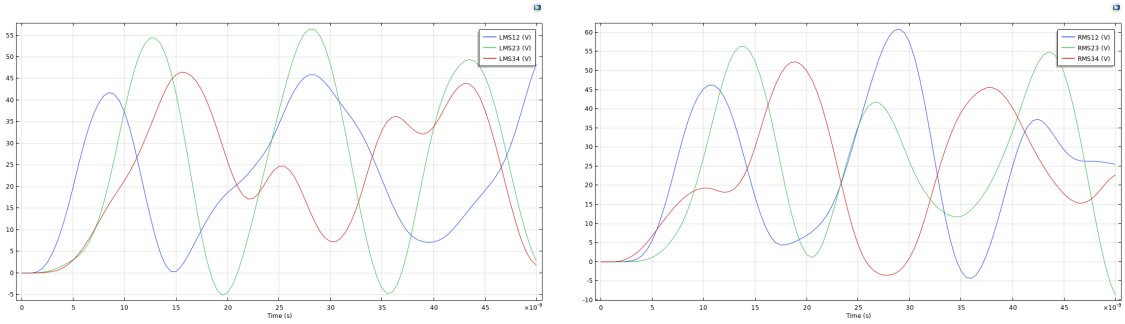

(a) Left mid-slot **(b)** Right mid-slot

Figure 5.12: Turn-to-turn voltages in the mid-slot

Figure 5.13 shows the turn-to-turn voltage measurements extracted from both overhangs in the winding. The close-side (CS) is the overhang between the input and ground slot. Hence, $CS12$ in figure 5.13a is quite similar to $RCS12$ in figure 5.11b, and $LCS23$ in 5.11a. The close-side overhang has the highest peak values at approximately 60 % of the voltage input. The far side (FS) overhang has similar t2t-voltages as the left mid-slot in figure 5.12a, where the voltage between turn 2 and 3 appear with the highest peak.

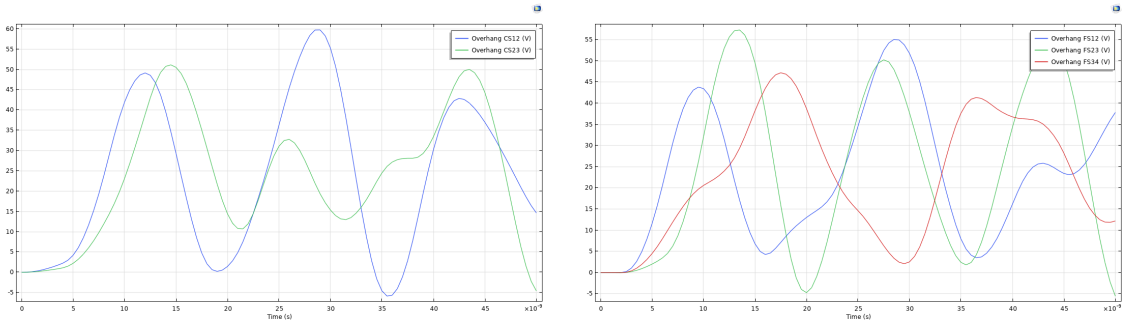

(a) close-side overhang **(b)** Far side overhang

Figure 5.13: Turn-to-turn voltages in the overhangs

5.2.2 8 – Turn Winding

Here, the FEM simulations of the 8-turn winding are presented. The same cases as in the analytical study have been examined, regarding different voltage input and grounding, T1 and T8. For the 8-turn winding, left and right close-side have been considered to extract t2g- and t2t-voltages. Figure 5.14 and 5.17 illustrate the location of voltage input and ground of the different cases. The numbers represent the turn in the respective slots, where the current directions of each conductor are denoted with x or dot, to symbolize the inward- and outward current direction, respectively.

Voltage input turn 1 (T1)

First, the T1 simulation result is presented. Figure 5.14 shows the location of the voltage input and ground, which can be seen in the right and left slot, respectively. The mainwall insulation is grounded similar to the 4-turn winding (grounding case D), where the sides and bottom are in contact with ground, as it would be if the winding was fitted in a stator core slot.

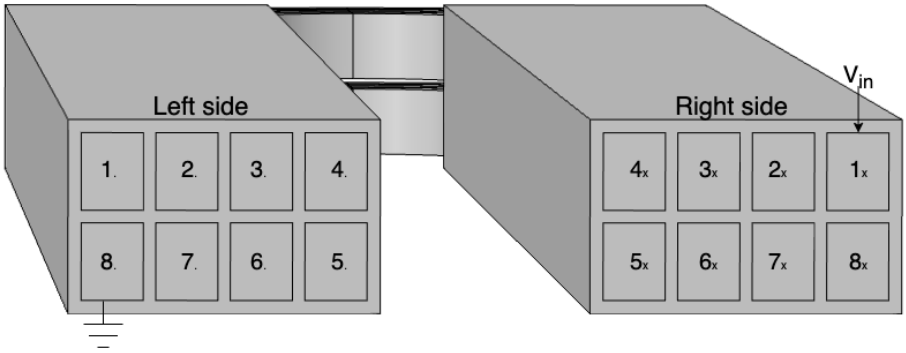

Figure 5.14: Slot explaination of T1 - Voltage input at turn 1 and turn 8 grounded

Figure 5.15a and 5.15b show the respective simulations from the left and right slot, where the left and right measurements are represented by L and R. The simulation time is 50 ns, which is five times the transition time of the step. The voltage signal oscillates back and forth within the winding due to many reflections. This could probably be the reason for the high peaks appearing in turn 2, 3 and 4, in both slots. Turn 1 – 4 have the highest peaks in both figures, while turn 5 – 8 have the lowest. Another notation is that $L80$ in figure 5.15a is not entirely grounded, which it should be. This could indicate insufficient grounding.

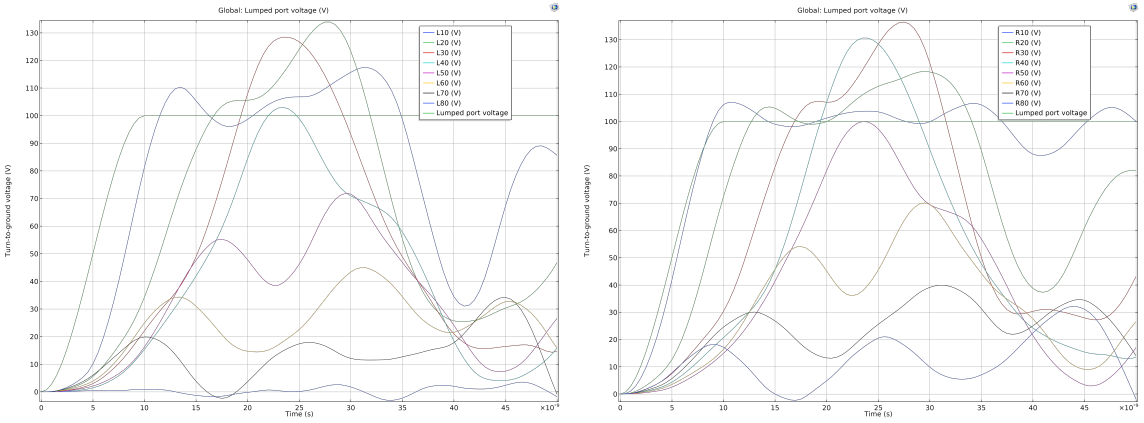

(a) Left slot (grounded) **(b)** Right slot (Voltage input)

Figure 5.15: Turn-to-ground voltages of left and right slot

Figure 5.16a and 5.16b show the simulated turn-to-turn voltages for adjacent turns in the left and right slot, respectively. The measurements from each respective slot are noted RCS and LCS, which represent the right close-side and the left close-side, concerning figure 5.14. Both figures have the highest voltage distributed over the vertically adjacent turns, which are between turn 1-8, 2-7, 3-6 and 4-5. Except for these, the highest peak is between turn 1-2, which is approximately 50 V.

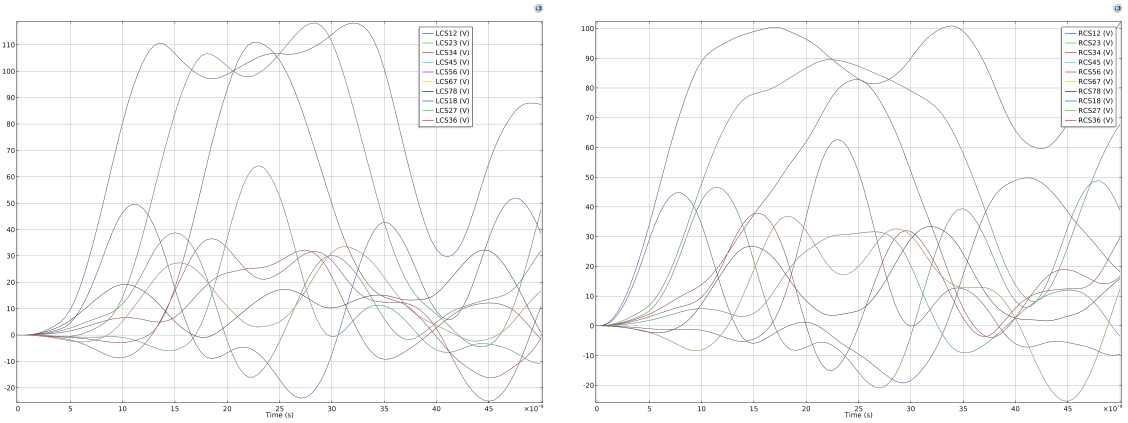

(a) Left slot (grounded) **(b)** Right slot (Voltage input)

Figure 5.16: Turn-to-turn voltages of left and right slot

Voltage input turn 8 (T8)

The T8 simulations will now be presented. Figure 5.17 depicts the locations of ground and voltage input, whereas the left slot contains the voltage input and right slot the grounded turn. The grounding of the mainwall insulation is the same as for T1, where the top of the mainwall is ungrounded. Thus, the voltage input is placed closer to ground in this case.

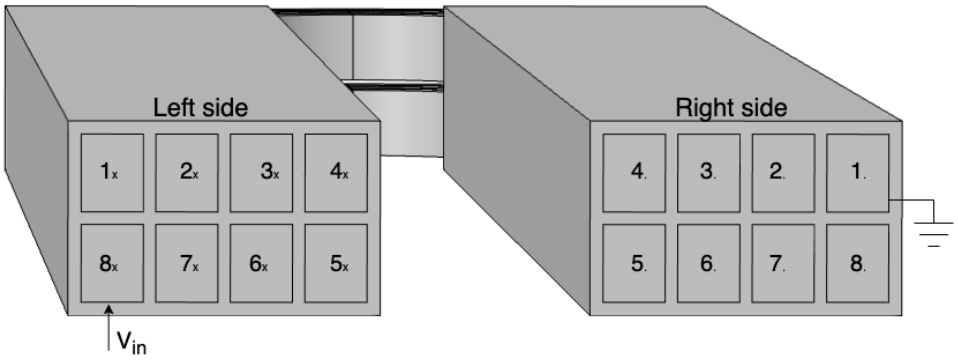

Figure 5.17: Slot explaination of T8 - Voltage input at turn 8 and turn 1 grounded

Figure 5.18a and 5.18b show the turn-to-ground measurements of the respective slots. The first four turns have the highest peaks here as well, where the turn connected to

voltage input is referred to as the first turn. The highest peak in the left slot is $L60$ and in the right slot $R70$. These are almost the same since $L60$ is located at the start of turn 6, and $R70$ at the end of turn 7. The peak value is above 150 V, which is a result of the reflections in the winding. The peak of the oscillation in the input turn is approximately 108 V, which can indicate that only small reflections reach turn 8. The grounding of $R10$ is similar to $L80$ of case T1; small oscillations occur in the last turn, which is supposed to be grounded.

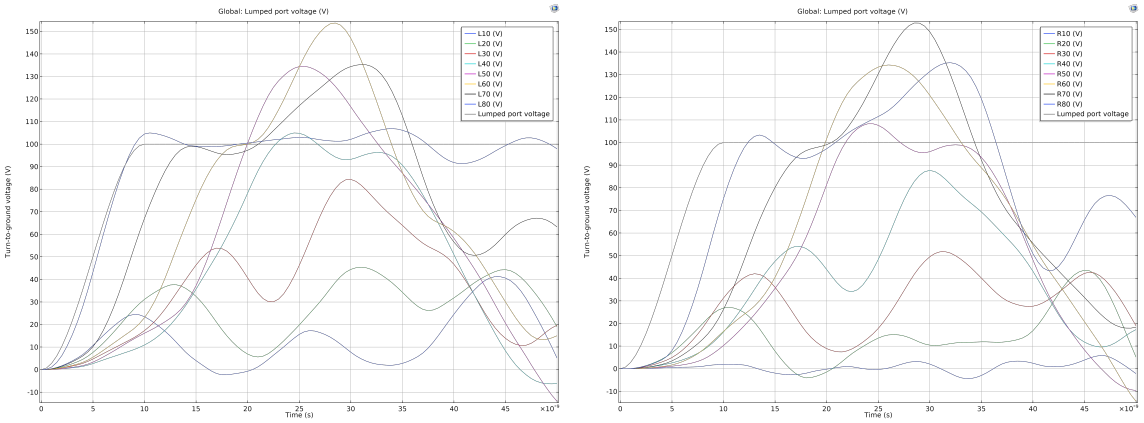

(a) Left slot (voltage input) **(b)** Right slot (grounded)

Figure 5.18: Turn-to-ground voltages of left and right slot

The turn-to-turn voltage simulations are shown by figure 5.19a and 5.19b. After the voltage step signal has reached steady-state, $t = 10$ ns, the oscillations in the winding keeps on reflecting back and forth, which distributes the voltage between the vertically adjacent turns to around 100 %.

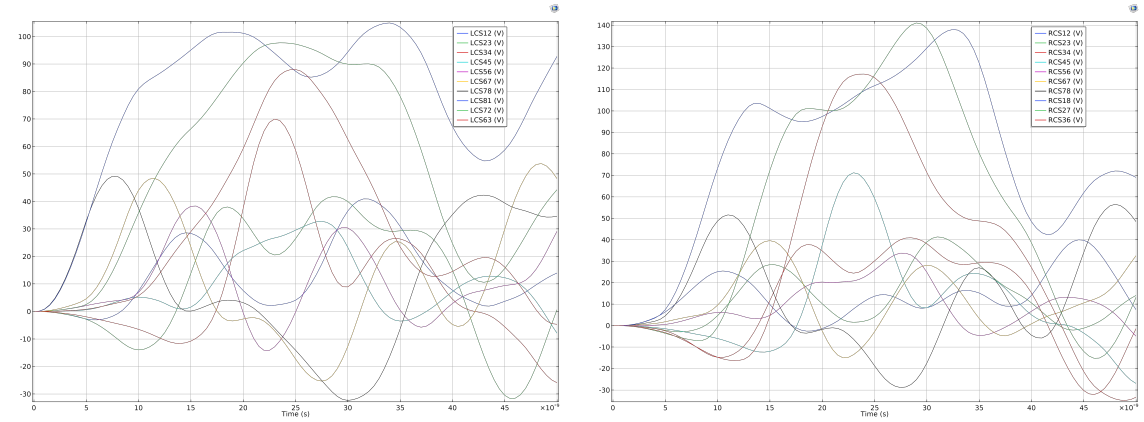

(a) Left slot (voltage input) **(b)** Right slot (grounded)

Figure 5.19: Turn-to-turn voltages of left and right slot

5.3 Comparison Analytical and FEM Model

Comparing the two different methods is challenging. The distribution of the FEM simulations are selected at the time instant where the step signal at the input flattens out, which is $t = 10\ ns$. Depending on where the measurements are extracted, the voltage at turn 1 will either have exceeded or not reached 100 % value of the step. Hence, the method used to compare these distributions is by converting the distribution to a percentage of the achieved voltage in turn 1 at $t = 10\ ns$. Both the left and right slot have been compared against the analytical distribution.

5.3.1 4 – Turn Winding

The comparisons of the two methods for the 4 turn winding will be given here. The focus here is to compare the base dimensions of analytic and FEM result. Followed by some parametric study result, such as the grounding cases and the maximum and minimum parameter value. This is done to compare the effect of change in parameters. Additionally, some special cases have been studied which combines two changed parameters, such as thick mainwall insulation and thin turn insulation, and $\varepsilon_{r,turn}$ and low $\varepsilon_{r,mainwall}$.

Base Dimensions

The turn-to-ground and turn-to-turn distribution of the base dimensions are shown and compared in figure 5.20a and 5.20b, respectively. The right slot distribution in the FEM model appears much more identical in form and value to the analytical distribution. The distribution of the left slot has the last turn unequal zero, due to the measuring at turn 4 is extracted at the start of the turn. Thus, the highest interturn voltage appears between turn 2 and 3.

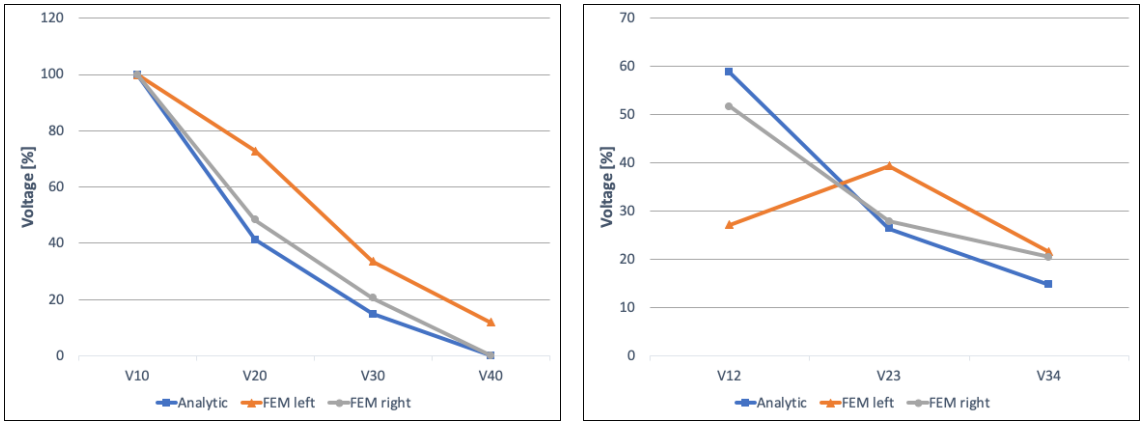

(a) Turn-to-ground distribution

(b) Turn-to-turn distribution

Figure 5.20: Comparison of analytical and FEM simulation distribution of the 4-turn winding with base dimensions

Grounding Cases

The different grounding scenarios have been simulated in both analytical and FEM for comparison.

Case A and B represent air coils with ground placed as shown in figure 5.1 and 5.2, respectively. The distribution in the left slot of Case A and B can be seen to have a different shape than the two other distributions. When comparing the analytical distribution to FEM, the distribution in the right slot is most identical. Based on the other comparisons, the voltage over the first two turns appears highest. However, this is not the case here. V_{12} is highest in the right slot of the FEM simulation for both case A and B.

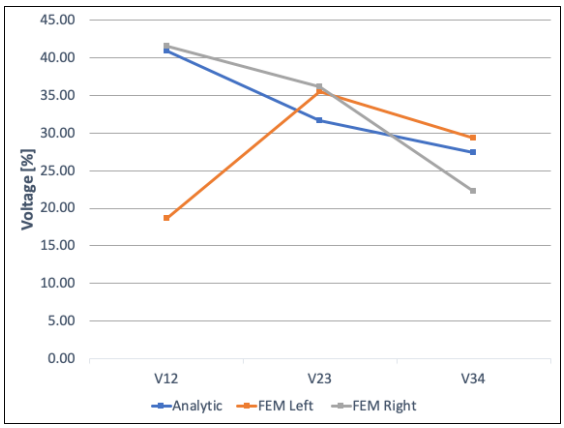

Figure 5.21: Comparison of grounding Case A

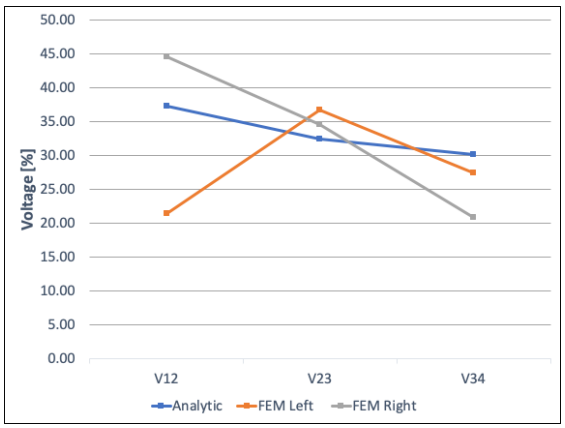

Figure 5.22: Comparison of grounding Case B

Case C and D represent coils in a stator core, where ground is as shown in figure 5.3 and 5.4. Case D is the most realistic with an open top that borders to air, whereas case C is enclosed by ground, mostly to see how this affects the voltage distribution. Case D is the grounding used in the base case and is, therefore, equal figure 5.20b. The difference of case C and D are barely visible in the FEM distributions, see figure 5.23 and 5.24. However, the analytical distribution has a distinct difference, especially V_{12}, where the distributed voltage decreases by 10 % by opening the top.

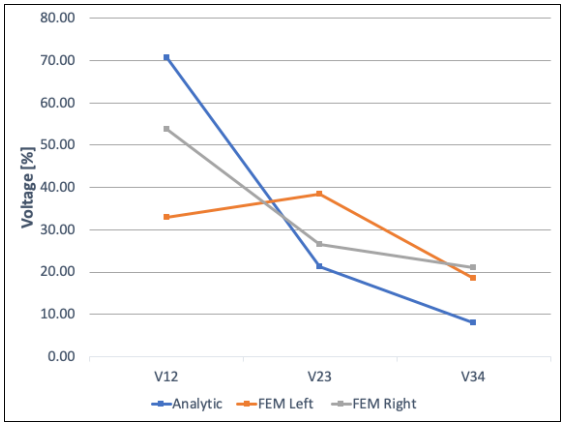

Figure 5.23: Comparison of grounding Case C

Figure 5.24: Comparison of grounding Case D

Case E and F are also unrealistic coils, primarily due to no mainwall insulation, where the purpose is to see the effect and compare it in the different methods. These cases have a similar effect as the two previous cases, C and D, where the FEM distribution have minor changes and the analytical distribution has significant changes, particularly over the first two turns.

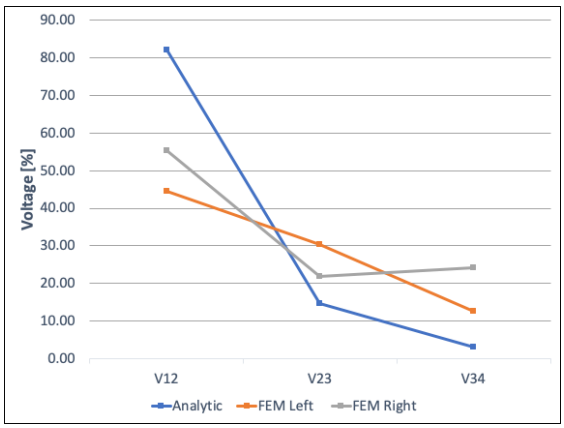

Figure 5.25: Comparison of grounding Case E

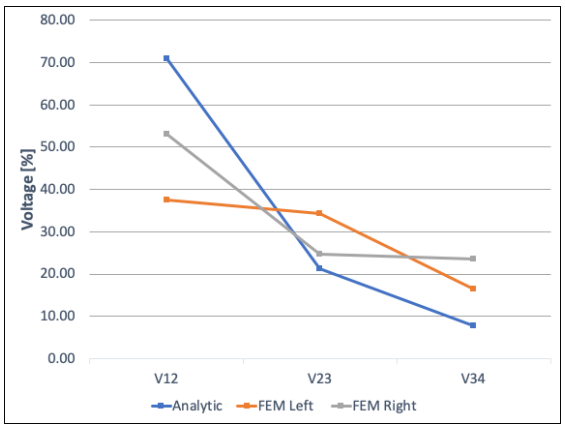

Figure 5.26: Comparison of grounding Case F

The different grounding scenarios can conclude that changing one ground boundary, has a minor effect in the FEM models, but a more significant effect in the analytical model. This can be seen in case C – F. Case A and B change from one ground boundary to four. Nevertheless, the effect is small in the FEM simulations, which also is true for the analytical distribution, where both methods have a maximum change of approximately 3 %.

Interturn Insulation Thickness

The parametric study has analyzed different interturn insulation thicknesses, where the capacitance and voltage distribution results are tabulated in table 5.4 and 5.5,

respectively. The cases with maximum and minimum interturn thickness have been simulated in FEM for the matter of comparison, which is presented here. Thus, the interturn thicknesses compared here are $\delta_t = 0.2\ mm$ and $\delta_t = 1.0\ mm$.

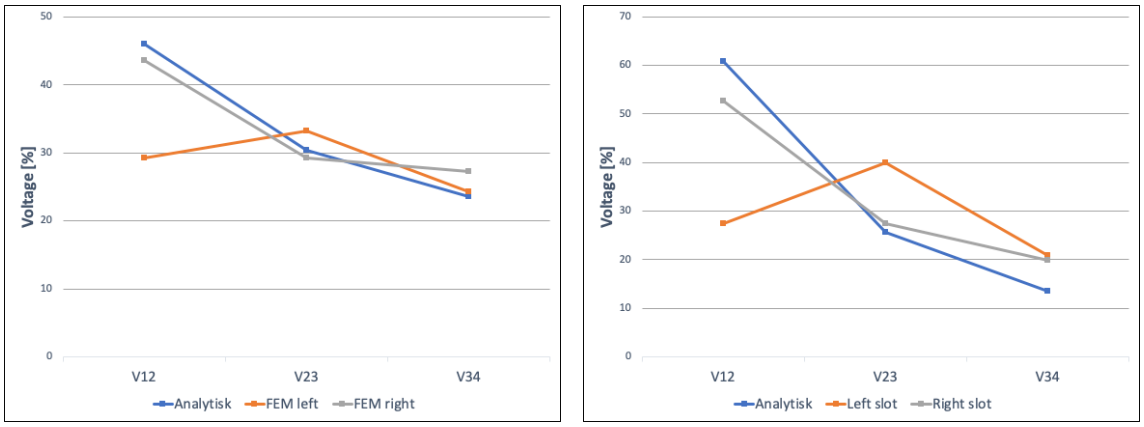

(a) $\delta_t = 0.2\ mm$ **(b)** $\delta_t = 1.0\ mm$

Figure 5.27: Comparison of analytical and FEM simulation distribution of max/min turn insulation thickness

Based on figure 5.27a and 5.27b, a thinner interturn thickness results in the right slot and analytical distribution becoming more identical. Oppositely, the right slot and analytical distribution differ more by increasing the interturn insulation thickness.

Mainwall insulation thickness

Mainwall insulation has also been examined for different thicknesses by the analytical parameter study. The max and min thicknesses have been simulated in FEM to compare the voltage distribution against the ones from the parameter study. Thus, the mainwall thicknesses compared here are $\delta_m = 0.25\ mm$ and $\delta_m = 0.65\ mm$. See figure 5.28a and 5.27b.

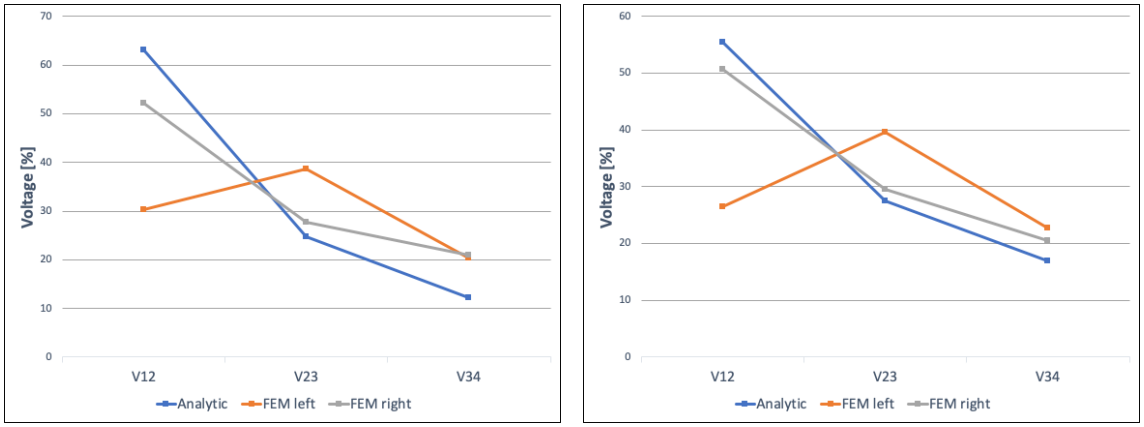

(a) $\delta_m = 0.25\ mm$ **(b)** $\delta_m = 0.65\ mm$

Figure 5.28: Comparison of analytical and FEM simulation distribution of max/min mainwall insulation thickness

It is known from table 5.9 that V_{12} decreases with increasing mainwall insulation thickness. The change of 0.25 mm and 0.65 mm results in a difference of 7.6 % in V_{12}. However, the FEM distributions change on a smaller scale, whereas V_{12} of the left and right slot differs by 3.8 % and 1.6 %, respectively. The distribution of the right slot is more identical to the analytical distribution for $\delta_m = 0.65\ mm$, and differs more by decreasing the mainwall insulation thickness.

Combination Cases

Some of the parameters that resulted in the best voltage distribution, individually, have been combined as an attempt to achieve a more idealized voltage distribution. The two cases studied here are:

- Thin turn insulation and thick mainwall insulation.
- High turn insulation permittivity and low mainwall permittivity.

Table 5.5 and 5.9 have shown that thin interturn insulation $\delta_t = 0.2mm$ and thick mainwall insulation $\delta_m = 0.65mm$ resulted in the most even distribution, respectively.

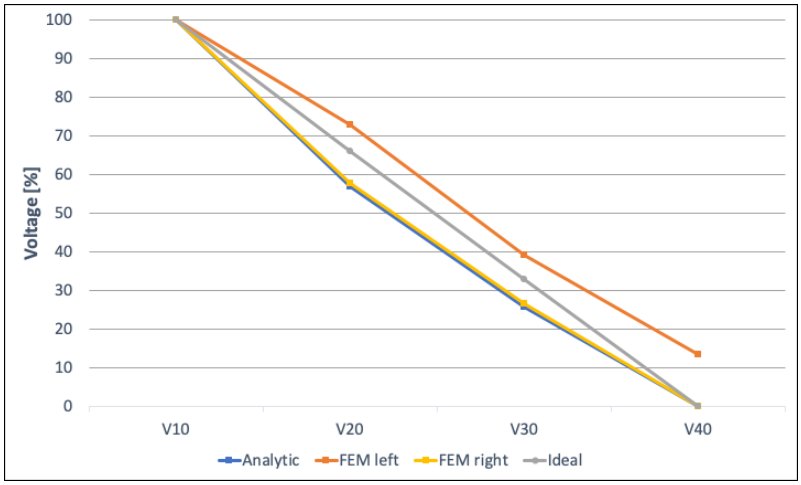

Figure 5.29: $\delta_t = 0.2\ mm$, $\delta_m = 0.65\ mm$

Figure 5.29 illustrates the voltage distribution of these two cases combined. An idealized voltage distribution is plotted as reference. The analytical and FEM distributions can be seen quite similar and close to ideal. Left slot in the FEM simulation is off due to the last turn, which is measured at the start, see figure 5.8.

Table 5.10 showed that the C_g/C_t-ratio did not differ due to equal changes in t2t- and t2g-capacitances with changing $\varepsilon_{r,turn}$. However, by decreasing $\varepsilon_{r,mainwall}$, the voltage distribution became more even, as shown in table 5.12.

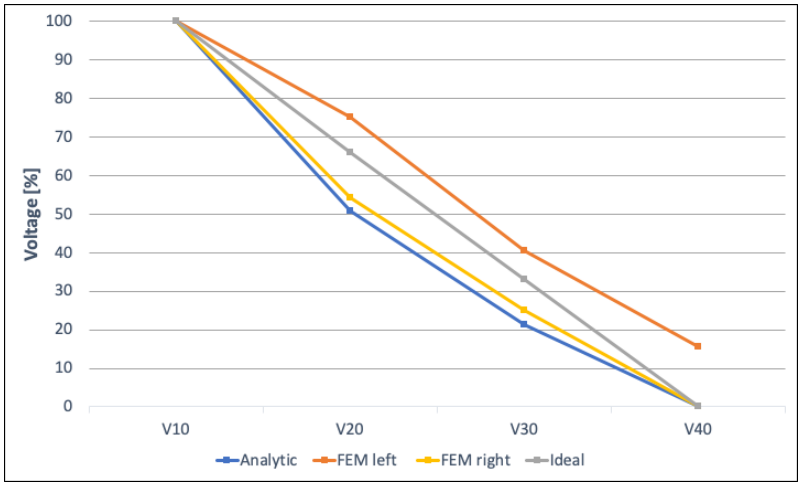

Figure 5.30: $\varepsilon_{r,turn} = 6$, $\varepsilon_{r,mainwall} = 2$

Figure 5.30 shows the voltage distribution of the case with high turn permittivity and low mainwall permittivity. Also here, an idealized voltage distribution is plotted as reference. The voltage distribution became more even with this combination than the one from table 5.12.

Additionally, theses two cases have been combined analytically. Table 5.17 shows a close to ideal distribution, where $\varepsilon_{r,turn} = 6$, $\varepsilon_{r,mainwall} = 2$, $\delta_t = 0.2\ mm$, $\delta_m = 0.65\ mm$.

Table 5.17: Voltage distribution [%] with $\varepsilon_{r,turn} = 6$, $\varepsilon_{r,mainwall} = 2$, $\delta_t = 0.2\ mm$, $\delta_m = 0.65\ mm$

V_{10}	V_{20}	V_{30}	V_{40}	V_{12}	V_{23}	V_{34}
100	62.6	30.1	0	37.4	32.5	30.1

5.3.2 8 – Turn Winding

Now, the comparisons of the analytical and FEM study will be given for the 8-turn winding. The focus here is mainly to compare the T1 and T8 case with base dimensions against the analytical distribution. The voltage distribution in the left and right slot of the FEM simulations have been extracted for comparison with the analytical distribution of table 5.14. Additionally, T1o and T8o are compared against the analytic distribution where the last turn is open. The goals are to find correlations between the methods and to find out which slot from the FEM simulations represent the analytical result best.

Voltage Input Turn 1

Comparisons of the different study methods will be examined here for T1 and T1o, separately. First, T1 comparison is presented, where the voltage signal is fed into turn

1 and turn 8 is grounded, see figure 5.14. Figure 5.31 illustrates the comparison of the analytical voltage distribution and the left and right slot distribution from the FEM simulation. The shape of the two FEM distributions appear surprisingly similar to the shape of the analytical study. The highest voltages of T1 are V_{18}, V_{12} and V_{27}, as shown by figure 5.31.

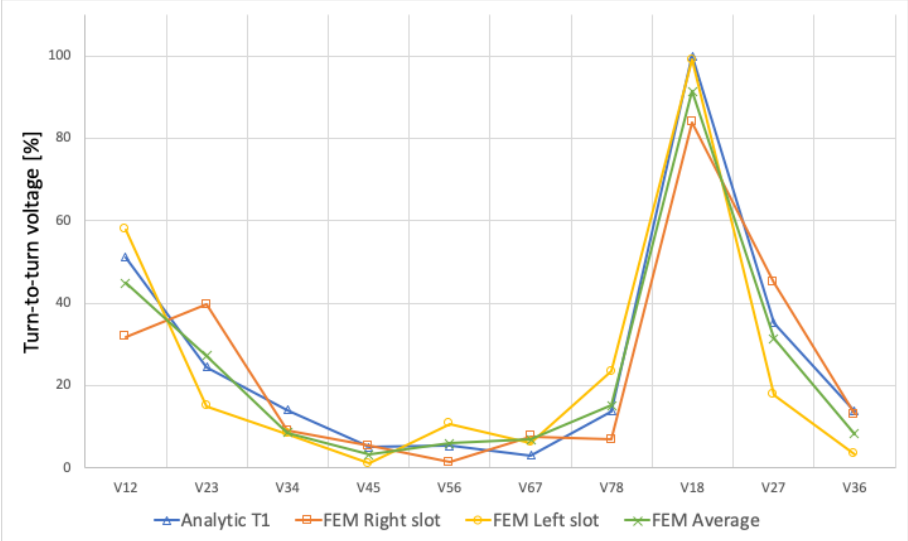

Figure 5.31: Comparison of analytical and FEM voltage distribution of T1

Both slot sides can be seen to vary around the analytical distribution. The average of these two FEM distributions have thus been plotted. Hence, the average distribution is more accurate regarding the analytic voltage distribution, where the highest difference is at V_{18}, which is 8.6 %.

Figure 5.32 shows the T1o voltage distribution of the analytical and FEM results, where the last turn is open. It can be seen by comparing figure 5.31 and 5.32 that the highest voltages in T1 have decreased in T1o, and the lowest voltages from T1 have increased in T1o. Thus, the voltage distribution of T1o is slightly more balanced than T1. Either way, the highest voltages of T1o are V_{18}, V_{12} and V_{27}.

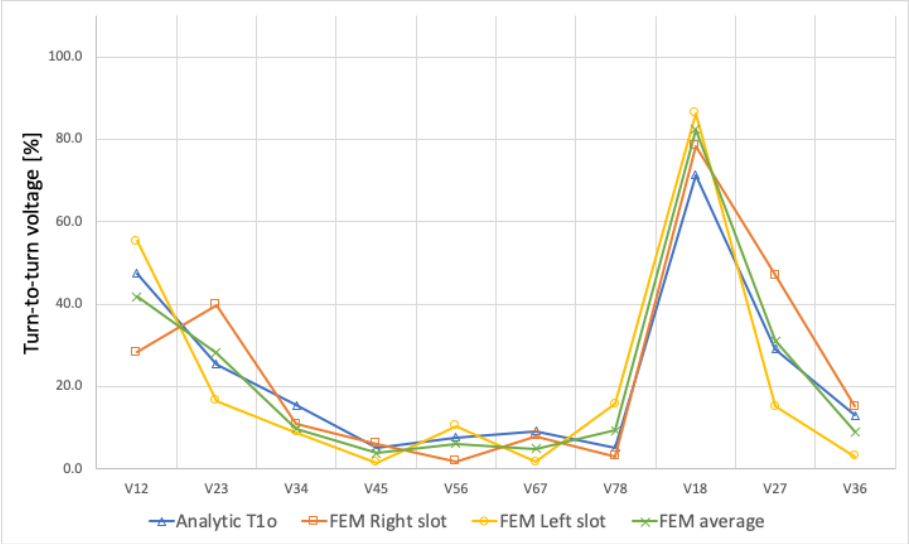

Figure 5.32: Comparison of analytical and FEM voltage distribution of T1o

The averaged FEM distribution has been plotted since both slot-sides vary around the analytical distribution. Not surprisingly, the average FEM distribution appears more accurate regarding the analytical result.

Voltage Input Turn 8

Comparisons of T8 and T8o will now be presented. First, T8 is the case where voltage input is located at turn 8 and turn 1 grounded, see figure 5.17. Similar to T1, both distribution shapes of the FEM simulation have some measurement points similar to the analytical distribution. The right slot distribution agrees most to the analytical distribution over the first four turns distributed from turn 8, while the left slot distribution is closest over the last four. See figure 5.33.

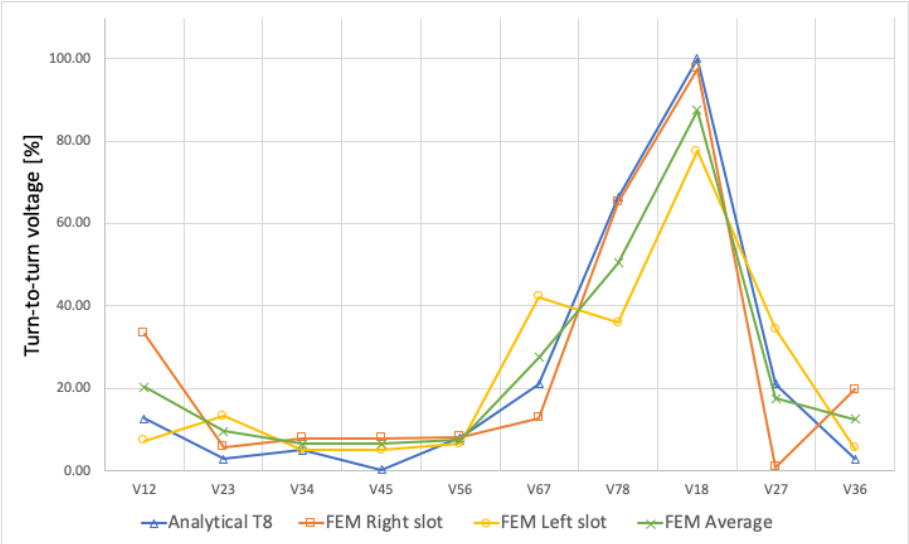

Figure 5.33: Comparison of analytical and FEM voltage distribution of T8

The highest voltages of T8 are V_{18}, V_{78}. The averaged FEM distribution aligns closest to the analytic distribution here also.

Figure 5.34 shows the comparison of T8o, where the last turn is open. In contrast to figure 5.33, it can be seen that the voltage distributions in figure 5.34 are more balanced.

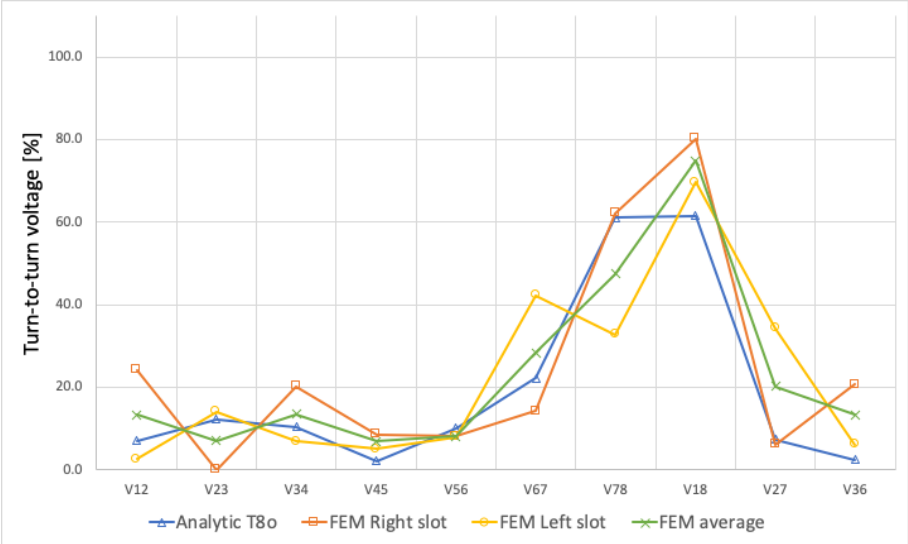

Figure 5.34: Comparison of analytical and FEM voltage distribution of T8o

Another observation is that V_{18} is not the highest as it has been in all the other cases, analytically. V_{18} and V_{78} are equally distributed regarding the analytical result. Anyhow, T8o appears to have the best voltage distribution compared to the other cases, where the highest voltages are V_{18} and V_{78} in the 60-70 % range, and all others below 25 %.

Chapter 6

Discussion

Towards commercial AEA, the technology must evolve within all aspects. One of the major factors needed to evolve is power density, which can increase by decreasing the volume and weight. This thesis focuses on the capacitive voltage distribution, which stresses the turn insulation. Analytical and FEM studies are used in this thesis to estimate the initial voltage distribution.

This chapter will reflect on four main discussion points. First, the main findings in the literature review are discussed, followed by a discussion of the findings from the parameter study. Next, a reflection around the comparisons of the two methods is given. This chapter concludes with a reflection of the validity of the results.

6.1 Main Findings from Literature Survey

The research towards commercial AEA continues to thrive. However, every change is a trade-off matter, where other problems may arise. Insulation systems are tailored to electric motors in specific applications. For instance, electric motors with HTS materials from [6] will need an insulation system with high thermal classification and cooling system with temperatures as low as liquid hydrogen, to avoid thermal breakdown. The aviation industry has high standards within safety precautions, which may demand more accuracy in the testing of equipment meant for AEA. The lifetime testing, according to IEC 60034-18-42, has been shown too optimistic [11, 12]. Based on the studies presented, it is thus recommended to test the whole coil with pulses similar to the ones it will be subjected to, to estimate the lifetime and PDIV.

One of the motivations for this thesis is to contribute to optimize the insulation system by proposing a insulation thickness. However, it is not that simple. The origin of the voltage stress is shown in chapter 3, where the overshoot voltage at the terminals are presented, in addition to the uneven voltage distribution. Both these two factors have to be considered to propose an optimized insulation thickness.

6.2 Parameter Study

The parameter study examined several parameters and cases to see how they affect the capacitive voltage distribution. The maximum and minimum parameters were simulated in FEM for comparison purposes. This way, the effect of change in both methods could be measured and compared. A reflection around the findings from the parameter study will be presented here.

6.2.1 Grounding Cases

4 – Turn Winding

The grounding cases showed that changing the location of ground made a significant difference, analytically. The grounding scenarios of case A and B can, in some way, correspond to the overhang section, which is often surrounded by air. Both these cases had close to linear voltage distribution since the t2g-capacitance was low. Case D represented a winding fitted in a stator core slot trace with an open top. By adding a ground boundary at the top, as in case C, the voltage distributed over the first two turns went from 59 % to 71 %, which is quite drastically. The last two cases, E and F, have no mainwall insulation, which is not realistic. However, the effect of having ground on such close hold was shown, which resulted in a voltage drop of 70-80 % over the first two turns.

6.2.2 Insulation Properties

The two insulation components considered in this thesis are mainwall and turn insulation, where the lattice is emphasized. The parameters varied here were the insulation thickness and permittivity. The parameters were examined one at a time. However, some of the parameter values were combined and investigated, such as thin turn insulation and thick mainwall insulation. In addition, a case with high turn insulation permittivity and low mainwall permittivity were examined.

Insulation Thickness

Table 5.5 showed that thicker insulation between turns resulted in a more uneven voltage distribution, while a thicker mainwall insulation resulted in a more even distribution. A higher C_g/C_t-ratio results in a more uneven voltage distribution. Thus, the t2g-capacitances needs to decrease and the t2t-capacitances increase. Turn-to-turn capacitances are increased by decreasing the interturn insulation thickness and increasing the permittivity. However, decreasing the interturn insulation will weaken the breakdown strength kV/mm, which can be fatal for certain overvoltages. Decreasing the t2g-capacitances can be done by increasing the distance to ground with thicker mainwall insulation thickness or decreasing the permittivity of the mainwall insulation. However, too thick insulation is not preferable, as it would lead to larger machines and lower transmission of heat.

The voltage distribution closest to an even distribution was that of $\delta_t = 0.2$, where each conductor is taped with only one layer of mica insulation. It was therefore interesting to see what the voltage distribution would become by combining the turn and mainwall insulation thicknesses that gave the best distribution individually. Figure 5.29 showed a much-improved voltage distribution. By combining the thicknesses and permittivities that gave the best results, the voltage distribution became more even analytically, as shown in table 5.17.

Additionally, more insulation wrapped around the first turn was examined. This was done to see how the voltage distributed over the first two turns changed by increasing the insulation. The result can be seen in table 5.7, where the voltage over the first two turns became higher for each insulation layer added. However, the stress subjected between the first two turns will most likely become less, by the measure of kV/mm.

Further reflections can be made around this. The windings in this thesis have rectangular copper wires, which is known to have relatively high slot fill factor. By considering additional layers of tape around the first turn gives the situation depicted in figure 6.1, whereas the red areas within the insulation are possible air voids and the graded red are possible lost slot space. Of course, this is a rough representation since the conductor corners are not fillet, according to IEC 60317-0-2, but is intended for reflection.

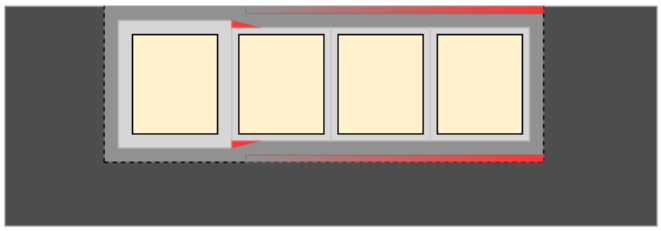

Figure 6.1: Rectangular copper wires with additional insulation around first turn

Figure 6.1 represents a cross-section of the 4-turn winding fitted in a stator core slot trace. The highlighted areas which can be problematic will change with different types of copper wire, such as round wires, or different types of insulation materials, such as varnish. Insulation fillers between the first two turns could also be an option. Either way, extra insulation can be sufficient to decrease the stress over the first two turns, but this will depend heavily on the configuration.

Insulation Permittivity

Different permittivity in the turn and mainwall insulation were examined one at a time. Analytically, the change in $\varepsilon_{r,turn}$ resulted in an equal difference for the t2t- and t2g-capacitances, which led to the same C_g/C_t-ratio in each case. Hence, the voltage distribution did not change. Changing $\varepsilon_{r,mainwall}$ however had insignificant change in the t2t-capacitances, but a larger difference in the t2g-capacitances. Thus, the voltage distribution changed with increasing mainwall permittivity, in an uneven manner.

By changing the permittivity of the air that surrounds the winding, other mediums impact on the voltage distribution can be examined. Oil-filled stators are used mainly in subsea systems due to its ability to sustain equilibrium in pressure. Aircraft motors will be subjected to different pressures, which decreases the PDIV in agreement with Paschen's curve [25]. Thus, a study was done by the analytical method where the permittivity of the surrounding material was changed to $\varepsilon_r = 2$, which represents oil. Analytically, the result became similar to the changing $\varepsilon_{r,turn}$, where the t2g- and t2t-capacitances changed equally, hence no difference in voltage distribution. However, this was also examined in FEM, as shown in table 6.1.

Table 6.1: Voltage distribution in % between 4-turn winding in oil-filled or air-filled stators

	V_{12}	V_{23}	V_{34}
FEM Air	51.7	27.9	20.4
FEM Oil	54.2	26.8	19.8

Only the distributions of the right slot have been examined since they became more representative for the 4-turn winding. The difference is not significant, which means it could be considered an advantage to have oil-filled stators with respect to PDIV and cooling, due to the thermal and ambient stresses the motor in an aircraft will be subjected to. Of course, further studies are necessary to draw conclusions around oil-filled versus air-filled stators in aircraft.

6.3 Comparison of Analytical and FEM

Chapter 5.3 presented the different comparisons between analytic and FEM voltage distributions. As expressed, comparing the two different methods is difficult, since the analytic approach is calculated electrostatically and FEM uses time-variant electric field calculations in its physics. Thus, the analytical model will have a stationary voltage distribution, while the FEM model will have reflections back and forth between the voltage input and ground. The selected method was to choose the time instant where the input signal flattens out since the theory behind the uneven voltage is based on the resulting characteristics from the steep front of the pulse. Other methods to compare the two studies could also have been done, such as comparing the peaks of the simulation results to the analytical results. However, if the reflection in the windings is incorrect, the ringing effect of the simulation will aggravate this error.

6.3.1 4 – Turn Winding

It can be concluded from the comparisons of the 4-turn winding in chapter 5.3, that the voltage distribution in the right slot (ground side) of the FEM simulation, is closest to the analytical voltage distribution. This is mostly because the right slot has the last turn grounded since it represents the end of the turns, while the left slot represents

the start of the turns, where the last turn is not zero. Thus, the distribution in the left slot appeared mostly with the highest voltage between turn 2 and 3, which resulted in a very different voltage distribution shape than the analytical and right slot. Generally, the discrepancies could be due to the simplifications made in both study methods.

The 4-turn winding is arguably too simple since it only has three possible turn-to-turn voltages to compare. However, the purpose of this simple winding was to see how some essential parameters affect the capacitive voltage distribution, analytically and in FEM.

The effect each parameter had was shown more significant in the analytical result. The FEM results were in agreement with the analytical result, but the magnitude of the changes was not equal. The comparisons of the grounding cases are good examples of the discrepancies of the two methods, whereas the analytical results showed a significant difference by adding an additional ground boundary, while the FEM results showed insignificant changes. This could be due to insufficient grounding of the main-wall insulation in FEM.

6.3.2 8 – Turn Winding

The more complex 8-turn winding has more t2t-voltages to compare, which makes it easier to see if the different methods are in agreement regarding the pattern of t2t-voltages. The voltage distribution from both slots was close to the analytical distribution. The averaged FEM distribution was closest in all four cases, which can indicate that the analytical voltage distribution is approximately equal to the averaged FEM distribution.

Four cases of the 8-turn winding were examined, where the goal was to find out which resulted in the worst voltage distribution. Both cases with the last turn grounded, T1 and T8, resulted in 100 % of the input voltage at V_{18}. T8 had 66 % of the incident voltage distributed over the first turns (V_{78}), while T1 had 51 % over the first turns (V_{12}), from the analytical results in table 5.14. The cases with last turn open, T1o and T8o, resulted in 71 % and 61 %, respectively, over the first and last turn V_{18}. These cases show how different the behaviour of a winding can be by changing the location of voltage input and ground.

6.4 Validation of the Results

Each winding design has different characteristics and response when measuring the voltage distribution. The best way to validate the FEM and analytical results would be to test actual windings with the exact dimensions and grounding as the windings considered in this thesis. Preparation work was done to test the 8-turn winding in this thesis, which unfortunately, did not happen due to several causes. Anyhow, the best way of validating the results here are by comparing the two methods against each other to see if they respond similarly. From chapter 5.3, it could be seen that the two different methods were in agreement, especially for the 8-turn winding. The 4-turn winding had only three measuring points to compare, which the right slot appeared in agreement with the analytical results.

Chapter 7

Conclusion

The work presented in this master thesis examines the voltage stresses in converter-fed electric aviation motors. The scope is narrowed down to investigate the voltage distribution in windings subjected to voltage pulses with short rise times. The objectives were to build 3D coils in FEM-software to simulate the voltage distribution and compare it to an analytical voltage distribution, to see if there exist a correlation. The voltage distribution investigated considers such short rise times that only the capacitive coupling of the winding determines the voltage distribution.

The aviation industry may require stricter testing procedures for lifetime estimation of insulation systems meant for commercial AEA. IEC 60034-18-42 is shown too optimistic by [11, 12].

Two winding configurations were analyzed analytically and in FEM. The purpose of the 4-turn winding was mainly to do a parametric study to see how basic parameters such as insulation thickness, permittivity and different grounding affects the capacitive voltage distribution. The 8-turn winding is a more complex configuration, where four different cases were developed with different voltage input and grounding. The purpose of this was to see which gave the worst voltage distribution. Also, additional insulation between the two layers in the 8-turn winding, interlayer insulation, was investigated for a few thicknesses, to see the impact it had on the voltage distribution.

Comparisons of the analytical and FEM study revealed a correlating effect. The analytical voltage distribution was best represented by averaging the FEM voltage distribution of the two slot sections.

The voltage distribution improved by decreasing the turn insulation thickness and mainwall insulation permittivity, and increasing the mainwall insulation thickness and turn insulation permittivity. The changes in these cases were confirmed by comparisons of FEM simulations, where the maximum and minimum parameter were simulated. However, to propose the required insulation thickness to withstand the voltage stresses, further investigations are needed. The breakdown strength has to be calculated by considering both the overshoot from the cable and rise time, and the uneven voltage distribution.

Chapter 8

Further work

This is a relatively new problem with several interesting aspects to research. Every aspect within an electric propulsion system will have to be optimized regarding weight and power. further towards an optimum. There are several tasks that is considered for further work:

- More complex analytical model which includes losses, skin- and proximity effects.
- Breakdown strength calculations to determine an optimized insulation thickness
- Test real windings in laboratory for validation of FEM and analytical.
- FEM simulation of a complete phase with PWM-like voltages at the winding terminal and a cable model between. Similar investigations for a complete 3-phase motor.

Bibliography

[1] EU, *Reducing emissions from aviation*, Accsessed: 10.06.20. [Online]. Available: https://ec.europa.eu/clima/policies/transport/aviation_en.

[2] R. Alexander, D. Meyer and J. Wang, 'A comparison of electric vehicle power systems to predict architectures, voltage levels, power requirements, and load characteristics of the future all-electric aircraft', in *2018 IEEE Transportation Electrification Conference and Expo (ITEC)*, 2018, pp. 194–200.

[3] B. Sarlioglu and C. T. Morris, 'More electric aircraft: Review, challenges, and opportunities for commercial transport aircraft', *IEEE Transactions on Transportation Electrification*, vol. 1, no. 1, pp. 54–64, 2015.

[4] K. F. Klaussen, 'Voltage stresses in converter-fed electric aviation motors - a literature review', [UNPUBLISHED] Department of Electric Power Engineering, NTNU, Dec. 2019.

[5] P. Wheeler, 'Technology for the more and all electric aircraft of the future', in *2016 IEEE International Conference on Automatica (ICA-ACCA)*, 2016, pp. 1–5.

[6] K. Kovalev, J. Nekrasova, N. Ivanov and S. Zhurzvlev, 'Design of all-superconducting electrical motor for full electric aircraft', in *2019 International Conference on Electrotechnical Complexes and Systems (ICOECS)*, 2019, pp. 1–5.

[7] A. Rufer, 'The dream of efficient energy storage — from bess, kers co to the hybrid power plant', in *2017 19th European Conference on Power Electronics and Applications (EPE'17 ECCE Europe)*, 2017, P.1–P.9.

[8] R. C. Bolam, Y. Vagapov and A. Anuchin, 'Review of electrically powered propulsion for aircraft', in *2018 53rd International Universities Power Engineering Conference (UPEC)*, 2018, pp. 1–6.

[9] T. Yu, J. Fu, R. Cai, A. Yu and Z. Chen, 'Nonprecious electrocatalysts for li?air and zn?air batteries: Fundamentals and recent advances.', *IEEE Nanotechnology Magazine*, vol. 11, no. 3, pp. 29–55, 2017.

[10] I. 60034-18-42, *Rotating electrical machines Part 18-42: Partial discharge resistant electrical insulation systems (Type II) used in rotating electrical machines fed from voltage converters, Qualification tests*. International Electrotechnical Commission, 2017.

[11] D. E. Moghadam, J. Speck, S. Grossmann and J. Stahl, 'Introducing of a test sample for iec/ts 60034-18-42 to assess the durability of the turn insulation', in *2018 IEEE 2nd International Conference on Dielectrics (ICD)*, Jul. 2018, pp. 1–5.

[12] P. Wang, A. Cavallini and G. C. Montanari, 'Endurance testing of rotating machines insulation systems: Do sinusoidal and square voltage waveforms provide comparable results?', in *2013 IEEE International Conference on Solid Dielectrics (ICSD)*, Jun. 2013, pp. 310–313.

[13] M. S. Moonesan, S. Jayaram, E. Cherney, R. Omranipour and S. U. Haq, 'Analysis of times-to-failure of various turn insulations of form-wound coils under pwm voltage waveform', in *2013 IEEE Electrical Insulation Conference (EIC)*, 2013, pp. 187–190.

[14] F. Sahlén, G. Paulsson and E. Mårtensson, 'Life-time investigation of mica-based insulation for high voltage machines subjected to converter-like voltages', in *2016 IEEE Electrical Insulation Conference (EIC)*, 2016, pp. 460–463.

[15] N. Mohan, T. M. Undeland and W. P. Robbins, *Power electronics: converters, applications, and design*. Wiley India, 2007.

[16] E. Persson, 'Transient effects in application of pwm inverters to induction motors', *IEEE Transactions on Industry Applications*, vol. 28, no. 5, pp. 1095–1101, 1992.

[17] GAMBICA/REMA, *Variable speed drives and motors - Motor Insulation Voltage Stress Under PWM Inverter Operation*, 1st. 2000.

[18] A. von Jouanne and P. Enjeti, 'Design considerations for an inverter output filter to mitigate the effects of long motor leads in asd applications', in *Proceedings of Applied Power Electronics Conference. APEC '96*, vol. 2, Mar. 1996, 579–585 vol.2.

[19] M. Kaufhold, H. Aninger, M. Berth, J. Speck and M. Eberhardt, 'Electrical stress and failure mechanism of the winding insulation in pwm-inverter-fed low-voltage induction motors', *IEEE Transactions on Industrial Electronics*, vol. 47, no. 2, pp. 396–402, Apr. 2000.

[20] M. Kaufhold, G. Borner, M. Eberhardt and J. Speck, 'Failure mechanism of the interturn insulation of low voltage electric machines fed by pulse-controlled inverters', *IEEE Electrical Insulation Magazine*, vol. 12, no. 5, pp. 9–16, 1996.

[21] M. Fenger, S. R. Campbell and J. Pedersen, 'Motor winding problems caused by inverter drives', *IEEE Industry Applications Magazine*, vol. 9, no. 4, pp. 22–31, 2003.

[22] G. Stone, I. Culbert, E. Boulter and H. Dhirani, "*Electrical insulation for rotating machines: design, evaluation, aging, testing, and repair*", 2nd. WILEY, 2014, ch. 1.

[23] D. E. Moghadam, J. Speck, S. Grossmann and J. Stahl, 'Voltage distribution in the stator windings of high voltage motors fed by pwm drives part i: Effects of the pulse characteristics', in *2018 IEEE 2nd International Conference on Dielectrics (ICD)*, Jul. 2018, pp. 1–4.

[24] D. E. Moghadam, J. Speck, S. Grossmann and J. Stahl, 'Voltage distribution in the stator windings of high voltage motors fed by pwm drives part ii: Considering the coil arrangements', in *2018 IEEE 2nd International Conference on Dielectrics (ICD)*, 2018, pp. 1–4.

[25] C. Abadie, T. Billard and T. Lebey, 'Partial discharges in motor fed by inverter: From detection to winding configuration', *IEEE Transactions on Industry Applications*, vol. 55, no. 2, pp. 1332–1341, Mar. 2019.

[26] D. E. Moghadam, J. Speck, S. Grossmann and J. Stahl, 'Parameters affecting the turn insulation lifetime and durability', *IEEE Transactions on Dielectrics and Electrical Insulation*, vol. 25, no. 2, pp. 516–523, 2018.

[27] P. K. Olsen, *Insulation system for rotating machines - analysis of an offshore wind turbine generator*, NTNU, Trondheim, 2008.

[28] L. Lusuardi, A. Cavallini, M. G. de la Calle, J. M. Martínez-Tarifa and G. Robles, 'Insulation design of low voltage electrical motors fed by pwm inverters', *IEEE Electrical Insulation Magazine*, vol. 35, no. 3, pp. 7–15, May 2019.

[29] S. Friedel, *How to calculate a capacitance matrix in comsol multiphysics®*, Accsessed: 25.04.20, Jun. 2017. [Online]. Available: https://www.comsol.com/blogs/how-to-calculate-a-capacitance-matrix-in-comsol-multiphysics/.

[30] J. M. Martinez Tarifa, *Transient voltage distribution along lv motor windings fed with pwm converters. insulation ageing analysis*, [PhD Thesis] Department of Electrical Engineering, Universidad Carlos III of Madrid, 2005.

[31] W. Frei, *Computational electromagnetics modeling, which module to use?*, Accsessed: 12.03.20, Sep. 2013. [Online]. Available: https://www.comsol.com/blogs/computational-electromagnetics-modeling-which-module-to-use/.

[32] A. Krings, G. Paulsson, F. Sahlén and B. Holmgren, 'Experimental investigation of the voltage distribution in form wound windings of large ac machines due to fast transients', in *2016 XXII International Conference on Electrical Machines (ICEM)*, 2016, pp. 1700–1706.

[33] W. Frei, *Modeling of coplanar waveguides*, Accsessed: 18.05.20, Jun. 2013. [Online]. Available: https://www.comsol.com/blogs/modeling-coplanar-waveguides/.

[34] COMSOL, *Rf module - user's guide*, COMSOL Multiphysics®, 2018. [Online]. Available: https://doc.comsol.com/5.4/doc/com.comsol.help.rf/RFModuleUsersGuide.pdf.

[35] W. Frei, *Modeling metallic objects in wave electromagnetics problems*, Accsessed: 20.03.20, May 2015. [Online]. Available: https://www.comsol.com/blogs/modeling-metallic-objects-in-wave-electromagnetics-problems/.

[36] W. Frei, *Ports and lumped ports for wave electromagnetics problems*, Accsessed: 05.05.20, Mar. 2015. [Online]. Available: https://www.comsol.com/blogs/ports-and-lumped-ports-for-wave-electromagnetics-problems/.

[37] H. Gothäll, *How to inspect your mesh in comsol multiphysics®*, Accsessed: 09.04.20, May 2017. [Online]. Available: `https://www.comsol.com/blogs/how-to-inspect-your-mesh-in-comsol-multiphysics/`.

[38] H. K. Høidalen, *TET 4130 Overspenninger og overspenningsvern*. Department of Electric Power Engineering, NTNU, 2017, pp. 121–124.

Appendix A

Analytical Formulas

A.1 Maxwell's Equations

Maxwell's equation governs the electromagnetic fields in a medium.

$$\nabla \cdot \boldsymbol{D} = \rho \tag{A.1}$$
$$\nabla \cdot \boldsymbol{B} = 0 \tag{A.2}$$
$$\nabla \times \boldsymbol{E} = -\frac{\partial \boldsymbol{B}}{\partial t} \tag{A.3}$$
$$\nabla \times \boldsymbol{H} = \boldsymbol{J} + \frac{\partial \boldsymbol{D}}{\partial t} \tag{A.4}$$

Formulations for high-frequency waves can be derived from equation A.3 and A.4 by using the constitutive relations for linear materials:

$$\boldsymbol{D} = \varepsilon \boldsymbol{E} \tag{A.5}$$
$$\boldsymbol{B} = \mu \boldsymbol{H} \tag{A.6}$$
$$\boldsymbol{J} = \sigma \boldsymbol{E} \tag{A.7}$$

The Maxwell-Ampere's and Faraday's law can then be written as:

$$\nabla \times \boldsymbol{H} = \sigma \boldsymbol{E} + \varepsilon \frac{\partial \boldsymbol{E}}{\partial t} \tag{A.8}$$
$$\nabla \times \boldsymbol{E} = -\mu \frac{\partial \boldsymbol{H}}{\partial t} \tag{A.9}$$

A.2 Chain Capacitance

By knowing that the definition of capacity is

$$C = \frac{Q}{U}$$

equations for voltages and charge in each turn can be established. The voltage distribution in the transient period can be calculated by using the method described in [38], which is developed for chain of capacitances in transformer coils or insulator chain, which is similar in many ways. The distance, Δx between each turn are the same and known. For a known coil length l, the number of turns are $\frac{l}{\Delta x}$.
The charge in the adjacent turn to x can be found by

$$Q(x+\Delta x) = Q(x) + C_g \cdot u(x) \tag{A.10}$$

and

$$Q(x+\Delta x) = C_t \cdot (u(x+\Delta x) - u(x)) \tag{A.11}$$

Since $\Delta x \to 0$ it makes sense to express C_{tt1} and C_{tg1} as:

$$C_t = \frac{C_{t(res)\cdot\Delta x}}{l} \tag{A.12}$$

$$C_g = \frac{C_{g(res)} \cdot l}{\Delta x} \tag{A.13}$$

where $C_{t(res)}$ and $C_{g(res)}$ are the resultant capacitance between turns and turn to ground, respectively. Implementing these in eq.A.10 and A.11 yields:

$$\frac{Q(x+\Delta x) - Q(x)}{\Delta x} = C_t \cdot u(x) \tag{A.14}$$

$$Q(x+\Delta x) = C_t \cdot \frac{u(x+\Delta x) - u(x)}{\Delta x} \tag{A.15}$$

$\Delta x \to 0$ gives

$$\frac{dQ}{dx} = C_g \cdot u \tag{A.16}$$

$$Q = C_t \cdot \frac{du}{dx} \tag{A.17}$$

Which gives a second degree differential equation by implementation

$$\frac{d^2u}{dx^2} - \frac{C_g}{C_t} - u = 0 \tag{A.18}$$

The general solution can then be expressed as:

$$u(x) = A \cdot sinh(\alpha \cdot x) + B \cdot cosh(\alpha \cdot x) \tag{A.19}$$

where

$$\alpha = \sqrt{\frac{C_g}{C_t}} \tag{A.20}$$

By grounding the coil at $x = 0$ and voltage input U_0 are applied at $x = l$, the voltage distribution through the coil is given:

$$u(x) = U_0 \frac{sinh(\alpha \cdot x)}{sinh(\alpha \cdot l)} \tag{A.21}$$

If the coil is open at the last turn, du/dx must be zero. The voltage distribution is then given by:

$$u(x) = U_0 \frac{cosh(\alpha \cdot x)}{cosh(\alpha \cdot l)} \tag{A.22}$$

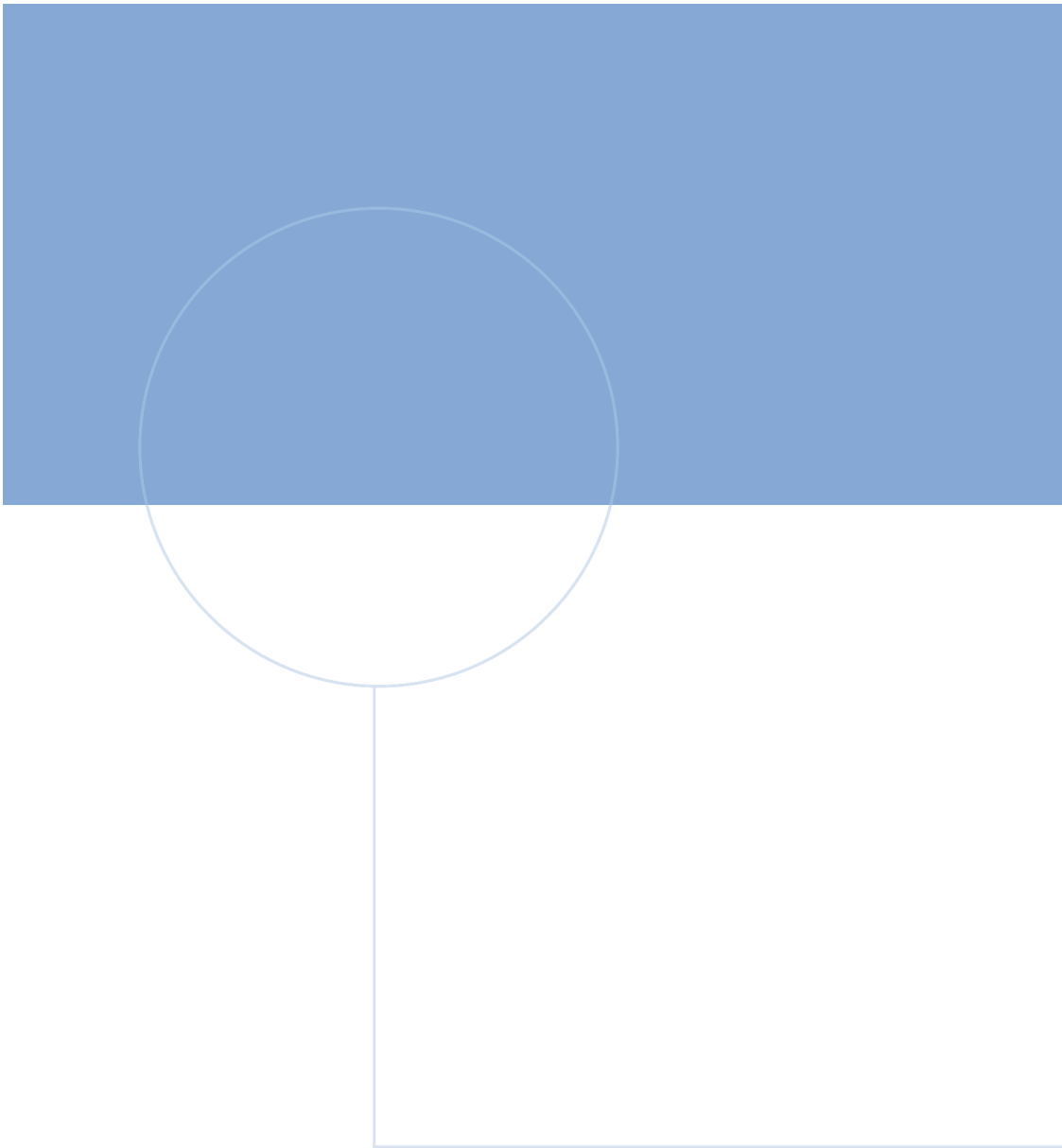

NTNU
Norwegian University of
Science and Technology